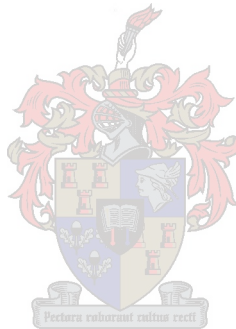


**TRANSVERSE AND LONGITUDINAL BOSE-EINSTEIN
CORRELATIONS IN ANTIPROTON-PROTON REACTIONS AT
CENTRE-OF-MASS ENERGY 630 GEV**

By

Faith Joy October



Thesis presented in partial fulfilment of the requirements for the degree of Master of Sciences
at the University of Stellenbosch.

Supervisor : Professor H.C. Eggers

March 2002

DECLARATION

I, the undersigned, hereby declare that the work contained in this thesis is my own original work and that I have not previously in its entirety or in part submitted it at any university for a degree.

Transverse and longitudinal Bose-Einstein correlations in $\bar{p}p$ reactions at

$\sqrt{s}=630$ GeV

Faith October

University of Stellenbosch

March 2002

ABSTRACT

We use Hanbury-Brown Twiss interferometry to determine Bose-Einstein correlations in the transverse and longitudinal directions. By using these two directions, we are able to determine the shape of the pion emitting source. The analysis is done with the UA1 (1985) data for $\bar{p}p$ collisions at $\sqrt{s} = 630$ GeV. Two frames of reference, namely the laboratory frame and the Longitudinal Center-of-Mass System (LCMS) are used. A fit to a two-dimensional Gaussian parametrization yields good results.

In the laboratory frame, an oblate form of the source is observed, with the value of the transverse radius (r_t) larger than the longitudinal (r_l) one. The LCMS analysis finds a prolate form of the source ($r_t < r_l$). A few reasons are discussed for the difference in the shape between the different reference frames. Our results are also compared with other hadron-hadron and e^+e^- experiments.

Transversale en longitudinale Bose-Einstein korrelasies in $\bar{p}p$ reaksies by

$\sqrt{s}=630$ GeV

Faith October

Universiteit van Stellenbosch

Maart 2002

OPSOMMING

Hanbury-Brown Twiss interferometrie was gebruik om Bose-Einstein korrelasies in die transversale en longitudinale rigtings te bepaal. Deur hierdie twee rigtings te gebruik, kan die vorm van die pion-bron bepaal word. Die UA1 (1985) datastel van die $\bar{p}p$ botsings by $\sqrt{s} = 630$ GeV is gebruik om die analise uit te voer. Twee verwysingstelsels, naamlik die laboratorium stelsel en die Longitudinale Massamiddelpunt-stelsel is aangewend. 'n Passing met 'n twee-dimensionele Gaussiese parametrisering het goeie resultate opgelewer.

In die laboratorium stelsel, is 'n ovaalvormige vorm vir die bron waargeneem, met die transversale radius (r_t) groter as die longitudinale radius (r_l). Die Longitudinale Massamiddelpunt stelsel het 'n prolate vorm vir die bron voorspel, met $r_t < r_l$. 'n Paar redes vir die verskil in die vorm van die pion-bron vir die verskillende verwysingstelsels word bespreek. Ons resultate word ook met ander hadron-hadron en e^+e^- eksperimente vergelyk.

ACKNOWLEDGEMENTS

Without God, it would have been impossible for me to complete this thesis.

I am at a lost for words to express my sincere thanks to professor H. C. Eggers for his commitment and encouragement to help me through my M.Sc studies. The enthusiasm and great insight he has in his field of study, made him the ideal person to work with.

I also want to convey my utmost gratitude towards Brigitte Buschbeck for the enormous part she played in assisting, advising and discussing the experimental work, which forms a crucial part of my thesis.

My dear boyfriend Stanley, who sat up with me and encouraged me time after time, was a great help. He also had to take the punch sometimes when I got too frustrated with the work. I am very thankful towards him.

I thank my parents and family for their understanding through difficult times and their moral support and prayers I could always rely on.

Last but not least, I want to thank everybody at the Physics department who helped in some way or another to make my years of study very enjoyable.

Financial assistance came from the National Rerearch Foundation and Postgraduate Bursaries (University of Stellenbosch).

John 1:3 (Amplified)

*“All things were made and came into existence through Him;
and without Him
was not even one thing made
that has come into being.”*

CONTENTS

ABSTRACT	iii
OPSOMMING	iv
ACKNOWLEDGEMENTS	v
1. INTRODUCTION	1
2. THE BOSE-EINSTEIN EFFECT	3
2.1 Bose-Einstein correlations	3
2.1.1 Origin	3
2.1.2 Quantum Statistics and Symmetrization	4
2.1.3 Density matrix approach	7
2.2 Experimental determination of C_2	9
2.2.1 Relation to cross sections	9
2.2.2 Binning and correlation integrals	9
2.2.3 Normalization	13
2.3 Variables and LCMS	14
2.3.1 One-dimensional variables	14
2.3.2 Three-momentum	16
2.3.3 Transverse and longitudinal components	17
2.3.4 The longitudinal center-of-mass system	18
2.4 Parametrizations	20
2.4.1 Parametrizations in terms of four-momentum	21
2.4.2 Cartesian parametrization	21
2.4.3 Transverse-longitudinal parametrization	23
2.4.4 Yano-Koonin-Podgoretskii parametrization	24
2.4.5 Parametrizations used by UA1	25
3. THE EXPERIMENT	27
3.1 The UA1 detector	27
3.1.1 General features	27
3.1.2 The Central Detector	28
3.1.2.1 Construction	28
3.1.2.2 Detecting charged hadrons	29
3.1.3 Data acquisition and reconstruction	30
3.2 Data sample and analysis	33
3.2.1 The sample and cuts	33
3.2.2 Correlation-specific cuts	33
3.2.3 Normalization	35

4. RESULTS AND DISCUSSION	38
4.1 One-dimensional analysis	38
4.2 Two-dimensional $q_t - q_l$ analysis	47
4.2.1 Lab frame fits	48
4.2.2 LCMS fits	54
4.2.3 Comparison with other experiments	59
4.2.4 Space-momentum correlations and lengths of homogeneity	59
4.2.5 Source elongation and Lorentz transformations	61
5. CONCLUSIONS	62
5.1 The role of frames of reference	62
5.2 Some factors affecting source parameters	63
REFERENCES	65

CHAPTER 1 INTRODUCTION

Bose-Einstein correlations show an enhancement in the probability of identical, indistinguishable bosons from the same particle source. This effect occurs at small values of the variable used to determine the correlations. Bose-Einstein correlations (BEC) can be used in hadron-hadron, hadron-nucleus, nucleus-nucleus and e^+e^- reactions at very high energies, to determine the size and lifetime of the particle production region, also known as the source of pion emission.

If the correlation function is expressed in terms of the components of the three momentum difference \mathbf{q} in specific directions, the shape of the source can also be determined, as the investigations in different directions reveal more information on the source. The structure of the source can be used to understand the dynamics of the interactions.

Bose-Einstein correlations were first implemented in 1956 by Hanbury-Brown and Twiss [1, 2] in astronomy. The correlations between the detected intensities of the emitted photons were used to determine the diameters of stars. In 1959 Goldhaber, et al. [3] extended the application experimentally to particle physics. Pions were detected and the angular correlations between like charge and unlike charge pairs were calculated. BEC were evident in the like charge pair analysis, by enhancing the distribution for small pair angles. The radius of interaction, and hence the size of the pion sources, could be determined. Bose-Einstein correlations became a widespread phenomenon and new developments on theoretical, as well as experimental level emerged from it.

The correlation function got more attention as different theoretical parametrizations were developed and implemented to fit the experimental data. Experiments were improved to obtain better statistics and to make higher dimensional analyses possible. The experimental determination of the correlation function was also refined to exclude other effects which could influence the BEC effect. This opened a new field of study, in that models which predicted certain shapes and sizes, were developed and tested with experimental analyses.

In this analysis, we will study the data of final states arising out of $p\bar{p}$ collisions as measured by the UA1 experiment. The transverse and longitudinal components of the three momentum difference, q_t and q_l will be used to determine the shape of the pion emitting source in these two directions. The experimental correlations will be calculated using the correlation integral method. Two frames of reference, namely the laboratory frame and the Longitudinal Center-of-Mass System (LCMS) will be used to make useful comparisons.

In order to extract information on the source, a two-dimensional Gaussian parametrization will be fit to the data. Comparison with other hadron-hadron, e^+e^- and heavy ion experiments will be made.

The determination of the shape of the source of bosons gives the possibility to analyse the spatial and temporal characteristics of the hadronisation region. At the same time the effect of the different reference frames on the pion source dimensions can be checked. Previous analyses at low energies [4], assumed a spherical shape of the source in the lab system, but theoretical and experimental investigations in the LCMS observed an elongation of the pion source. The space-time development of a particle collision provides information to understand the underlying dynamics.

Bose-Einstein correlations and the implementation of the correlation function will be discussed in Chapter 2. Chapter 3 contains the experimental set-up and in Chapter 4 the results will be shown. Some discussion on the results will be given. The conclusion will be made in Chapter 5.

CHAPTER 2

THE BOSE-EINSTEIN EFFECT

2.1 Bose-Einstein correlations

2.1.1 Origin

The field of Bose-Einstein correlations originated in astronomy in the form of intensity interferometry. Hanbury-Brown and Twiss discovered in 1956 [1, 2] that by only measuring the correlation in light intensity between the frequency outputs of a detector, the diameter of stars could be determined. Knowledge of the relative phase between the two signals was not necessary, as the signals were not combined before detection. An experiment was conducted in which the correlation between fluctuations in the current from two cathodes was calculated, using classical electromagnetic theory. The two mirrors focused the reflected light from the stars onto the photocathodes. The intensity fluctuations in the anode currents were amplified and the outputs from the amplifiers multiplied. The average value of the product of the outputs from the amplifiers was recorded on a counter. The readings of this counter gave a direct measure of the correlation between the intensity fluctuations in the light received at the two mirrors. It was noted that the correlation was preserved in the process of photo-electric emission and occurred only when the cathodes were superimposed, but not when they were widely separated. This was known as the Hanbury-Brown and Twiss (HBT) effect. After some deliberation, Brown and Twiss [5] clarified that the HBT effect was a consequence of the “clumping” of photons (photons are bosons) and that from a particle point of view, it was a characteristic quantum effect, as bosons have the tendency to occupy the same state.

Goldhaber, Goldhaber, Lee and Pais observed the same effect in particle physics three years later (1959) [3] when they studied the annihilation of low energy anti-protons in a propane bubble chamber. The opening angle between the pion pairs was used to determine the correlations. A clear difference between the angular distribution for pion pairs of like charge than pairs of oppositely charged particles was noted. The simple statistical model of phase space did not make provision for such a difference, necessitating the introduction of a properly symmetrized wave function.

After 1960, a revolution occurred in the field of particle-particle correlation studies. Many developments were made both theoretically and experimentally which improved the determination of the correlations. Previously the full correlation with the N -particle (N is the total number of particles) final state was determined. The two-particle correlations were then obtained by symmetrizing the wave function of the final state separately with respect to pairs of particles [3].

Changing the analysis to considering inclusive processes

$$A + B \rightarrow \pi^\alpha(\mathbf{p}_1) + \pi^\alpha(\mathbf{p}_2) + X$$

where A, B are the colliding particles, the π^α 's are two identical particles and X means “anything else”, simplified matters considerably as now the N -particle final state is ignored and only the two-particle state corresponding to all possible pairs $\pi^\alpha(\mathbf{p}_1)$ and $\pi^\alpha(\mathbf{p}_2)$ is symmetrized.

In the UA1 experiment A and B correspond to a proton and an antiproton and α can be $+$ or $-$. Kopylov and Podgoretskii further proposed a formalism, the two-particle correlation function, to calculate the correlations in any model [6]. The determination of the correlations could hence be model-independent.

In astronomy a space-time formulation of the experiment was done. In hadronic processes the characteristic interaction times are very short, therefore the space-time description of the events has to be reconstructed by measurements in energy-momentum space. Energy-momentum correlations allow estimation of the characteristic dimensions and durations of the generation processes [6, 7, 8]. According to the uncertainty relations, the momentum is related to the characteristic size of the emission region and the energy couples to the time of emission.

Combining the different characteristics into a one-dimensional Lorentz invariant four-momentum difference Q^2 , made analyses a bit easier. BEC were dominant in the like charge pairs for small values of Q^2 , when the like charge pions and unlike charge pion pairs were compared [3]. It was also found that the rise of BEC at small Q^2 , was related to “intermittency” in hadron-hadron interactions [9]. Today, BEC analysis is widespread including the full range of colliding systems, including lepton-lepton, lepton-hadron, hadron-hadron, hadron-nucleus and nucleus-nucleus.

2.1.2 Quantum Statistics and Symmetrization

In hadron physics, the greatest interest attaches precisely to the properties of the system that emits the hadrons. Since states of the emitted particles are described quantum mechanically, the quantum mechanics of identical particles is relevant.

The principle of indistinguishability of identical particles by Messiah and Greenberg states [10]:

“Dynamical states that differ only by a permutation of identical particles cannot be distinguished by any observation whatsoever.”

In quantum statistics, identical, indistinguishable particles that obey Bose-Einstein statistics are called bosons. Bosons have a symmetric wave function with respect to particle exchange,

$$\psi_{a,b}(1, 2) = \frac{1}{\sqrt{2}} [\psi(\mathbf{x}_a, \mathbf{p}_1)\psi(\mathbf{x}_b, \mathbf{p}_2) + \psi(\mathbf{x}_b, \mathbf{p}_1)\psi(\mathbf{x}_a, \mathbf{p}_2)] = \psi_{\text{sym}}(1, 2), \quad (2.1)$$

where $\psi_{\text{sym}}(1, 2)$ is the total symmetric wave function and $\psi(\mathbf{x}_i, \mathbf{p}_j)$ ($i = a, b$ and $j = 1, 2$) means that particle j was emitted from position \mathbf{x}_i and detected with momentum \mathbf{p}_j . The indistinguishability of the particles implies that the same particle could also have been emitted from the other position \mathbf{x}_b with momentum \mathbf{p}_1 as indicated in Fig. 2.1. By interchanging the particles, the wave function still remains the same.

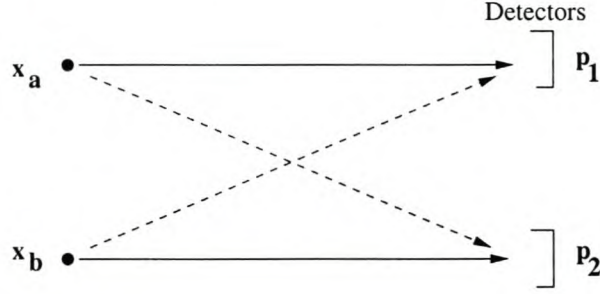


Figure 2.1: Experimental setup of two identical particles emitted at positions \mathbf{x}_a and \mathbf{x}_b . The momenta \mathbf{p}_1 and \mathbf{p}_2 are detected, but because of the symmetry of the wave function, it cannot be distinguished which particle came from which emitting point.

In hadronic collisions, the size of the source (the fireball just after the collision between the proton and anti-proton) is small and therefore the distance between the emission points \mathbf{x}_a and \mathbf{x}_b is also small ($|\mathbf{x}_a - \mathbf{x}_b| \approx 1\text{fm}$) compared to the distance from the source to the detector. This implies that the positions cannot be measured directly but only the momenta \mathbf{p}_1 and \mathbf{p}_2 .

If the source function can be described by a density distribution $\rho(\mathbf{x})$, normalized by $\int d^3\mathbf{x}\rho(\mathbf{x}) = 1$, then the symmetrized probability for measuring two momenta $(\mathbf{p}_1, \mathbf{p}_2)$ is given by

$$P_{12}(\mathbf{p}_1, \mathbf{p}_2) = \int d^3\mathbf{x}_a d^3\mathbf{x}_b \rho(\mathbf{x}_a)\rho(\mathbf{x}_b) |\psi_{\text{sym}}(1, 2)|^2. \quad (2.2)$$

The square of the wave function is:

$$|\psi_{\text{sym}}(1, 2)|^2 = \frac{1}{2} \{ |\psi(\mathbf{x}_a, \mathbf{p}_1)|^2 |\psi(\mathbf{x}_b, \mathbf{p}_2)|^2 + |\psi(\mathbf{x}_b, \mathbf{p}_1)|^2 |\psi(\mathbf{x}_a, \mathbf{p}_2)|^2 \} \\ + \psi^*(\mathbf{x}_a, \mathbf{p}_1)\psi^*(\mathbf{x}_b, \mathbf{p}_2)\psi(\mathbf{x}_b, \mathbf{p}_1)\psi(\mathbf{x}_a, \mathbf{p}_2). \quad (2.3)$$

If Eq. (2.3) and the normalization of the density is implemented, the probability reduces to

$$\begin{aligned}
 P_{12}(\mathbf{p}_1, \mathbf{p}_2) &= \frac{1}{2} \int d^3 \mathbf{x}_a \rho(\mathbf{x}_a) |\psi(\mathbf{x}_a, \mathbf{p}_1)|^2 \int d^3 \mathbf{x}_b \rho(\mathbf{x}_b) |\psi(\mathbf{x}_b, \mathbf{p}_2)|^2 \\
 &+ \frac{1}{2} \int d^3 \mathbf{x}_a \rho(\mathbf{x}_a) |\psi(\mathbf{x}_a, \mathbf{p}_2)|^2 \int d^3 \mathbf{x}_b \rho(\mathbf{x}_b) |\psi(\mathbf{x}_b, \mathbf{p}_1)|^2 \\
 &+ \int d^3 \mathbf{x}_a d^3 \mathbf{x}_b \rho(\mathbf{x}_a) \rho(\mathbf{x}_b) [\psi^*(\mathbf{x}_a, \mathbf{p}_1) \psi^*(\mathbf{x}_b, \mathbf{p}_2) \psi(\mathbf{x}_a, \mathbf{p}_2) \psi(\mathbf{x}_b, \mathbf{p}_1)],
 \end{aligned}$$

where the last term represents the interference effect.

In an idealised case, when the pions may be described by symmetrized plane waves (including the box normalization constant V),

$$\psi_{\text{sym}}(\mathbf{x}_a, \mathbf{x}_b, \mathbf{p}_1, \mathbf{p}_2) = \frac{V^{-1}}{\sqrt{2}} \left[e^{i(\mathbf{p}_1 \cdot \mathbf{x}_a + \mathbf{p}_2 \cdot \mathbf{x}_b)} + e^{i(\mathbf{p}_1 \cdot \mathbf{x}_b + \mathbf{p}_2 \cdot \mathbf{x}_a)} \right], \quad (2.4)$$

and if it is assumed that the individual pions were emitted with a pointlike spatial distribution of $\rho(\mathbf{x})$, then the number of pairs emitted with momentum $(\mathbf{p}_1, \mathbf{p}_2)$ is specifically given by

$$\mathcal{N}_{12}(\mathbf{p}_1, \mathbf{p}_2) = \int d^3 \mathbf{x}_a d^3 \mathbf{x}_b \rho(\mathbf{x}_a) \rho(\mathbf{x}_b) |\psi_{\text{sym}}(\mathbf{x}_a, \mathbf{x}_b, \mathbf{p}_1, \mathbf{p}_2)|^2. \quad (2.5)$$

Inserting Eq. (2.4) yields:

$$\begin{aligned}
 \mathcal{N}_{12}(\mathbf{p}_1, \mathbf{p}_2) &= \int d^3 \mathbf{x}_a d^3 \mathbf{x}_b \rho(\mathbf{x}_a) \rho(\mathbf{x}_b) \left| \frac{V^{-1}}{\sqrt{2}} \left[e^{i(\mathbf{p}_1 \cdot \mathbf{x}_a + \mathbf{p}_2 \cdot \mathbf{x}_b)} + e^{i(\mathbf{p}_1 \cdot \mathbf{x}_b + \mathbf{p}_2 \cdot \mathbf{x}_a)} \right] \right|^2 \\
 &= \frac{V^{-2}}{2} \int d^3 \mathbf{x}_a d^3 \mathbf{x}_b \rho(\mathbf{x}_a) \rho(\mathbf{x}_b) \left[2 + e^{-i(\mathbf{p}_1 \cdot \mathbf{x}_b + \mathbf{p}_2 \cdot \mathbf{x}_a - \mathbf{p}_1 \cdot \mathbf{x}_a - \mathbf{p}_2 \cdot \mathbf{x}_b)} \right. \\
 &\quad \left. + e^{-i(\mathbf{p}_1 \cdot \mathbf{x}_a + \mathbf{p}_2 \cdot \mathbf{x}_b - \mathbf{p}_1 \cdot \mathbf{x}_b - \mathbf{p}_2 \cdot \mathbf{x}_a)} \right] \\
 &= V^{-2} [1 + |\tilde{\rho}(\mathbf{p}_1 - \mathbf{p}_2)|^2],
 \end{aligned} \quad (2.6)$$

where $\tilde{\rho}(\mathbf{p}_1 - \mathbf{p}_2)$ is the Fourier transform of the distribution and depends on the relative momentum or the momentum difference $(\mathbf{p}_1 - \mathbf{p}_2) = \mathbf{q}$ only. If there is no interference, then the number of particles emitted with momentum \mathbf{p}_1 and momentum \mathbf{p}_2 respectively are

$$\begin{aligned}
 \mathcal{N}_1(\mathbf{p}_1) &= \int d^3 \mathbf{x}_a \rho(\mathbf{x}_a) |\psi_1(\mathbf{x}_a, \mathbf{p}_1)|^2 \\
 \mathcal{N}_2(\mathbf{p}_2) &= \int d^3 \mathbf{x}_b \rho(\mathbf{x}_b) |\psi_1(\mathbf{x}_b, \mathbf{p}_2)|^2.
 \end{aligned}$$

The product of these numbers, with the one particle wave function

$$\psi_1(\mathbf{x}_a, \mathbf{p}_1) = V^{-1/2} e^{i(\mathbf{p}_1 \cdot \mathbf{x}_a)},$$

inserted, is

$$\mathcal{N}_1(\mathbf{p}_1)\mathcal{N}_2(\mathbf{p}_2) = V^{-2}. \quad (2.8)$$

The correlation function of the two particles with interference, is the ratio between the number of pairs \mathcal{N}_{12} and the product of the single particle numbers $\mathcal{N}_1\mathcal{N}_2$. From Eqs. (2.7) and (2.8), the two-particle correlation function is given by

$$C_2(\mathbf{p}_1, \mathbf{p}_2) = \frac{\mathcal{N}_{12}}{\mathcal{N}_1\mathcal{N}_2} = 1 + |\tilde{\rho}(\mathbf{p}_1 - \mathbf{p}_2)|^2. \quad (2.9)$$

This is an essential result which states that [11]: “The probability of detecting two bosons depends on their relative momentum, with an enhancement equal to the square of the Fourier transform of the source distribution function.” The correlation function of two identical particles from a boson emitting source, can thus be derived by taking the symmetrized plane wave and computing the Fourier transform of the spatial distribution. Here the enhancement can be seen as the extra term $|\tilde{\rho}(\mathbf{p}_1 - \mathbf{p}_2)|^2$. In the special case that the density distribution is Gaussian, then the Fourier transform will also be Gaussian.

2.1.3 Density matrix approach

The above derivation represents a simplified caricature of the true particle production and symmetrization process. A better and general theory has been developed in terms of second quantization and density matrices.

Identical bosons are a subset of the particles produced, therefore they cannot be described by a pure wave function, but must rather be dealt with by a density matrix. The density matrix formalism quantitatively describes physical situations with mixed as well as pure ensembles. In this ansatz, the symmetry properties are expressed by the commutation relations of the creation and annihilation operators of particles [12]. The one- and two-particle distributions in terms of the momentum can thus be expressed as [13]

$$P_1(\mathbf{p}) = E \frac{dN}{d^3p} = E \langle \hat{a}_{\mathbf{p}}^\dagger \hat{a}_{\mathbf{p}} \rangle \quad (2.10)$$

and

$$P_2(\mathbf{p}_1, \mathbf{p}_2) = E_1 E_2 \langle \hat{a}_{\mathbf{p}_1}^\dagger \hat{a}_{\mathbf{p}_2}^\dagger \hat{a}_{\mathbf{p}_2} \hat{a}_{\mathbf{p}_1} \rangle, \quad (2.11)$$

where the angle-brackets denote the expectation value of an operator, described by the trace of

the product of the density matrix ρ and the operator:

$$\langle \hat{a}_{\mathbf{p}}^\dagger \hat{a}_{\mathbf{p}} \rangle = \text{Tr}(\rho \hat{a}_{\mathbf{p}}^\dagger \hat{a}_{\mathbf{p}}).$$

This is a powerful tool in determining the distributions, as the trace is independent of the basis and any convenient basis can thus be used.

As $\hat{a}_{\mathbf{p}}^\dagger \hat{a}_{\mathbf{p}} = \hat{N}$ is the number operator, P_1 just counts the average number of pions with momentum \mathbf{p} and P_2 counts the average number of pion pairs with momenta \mathbf{p}_1 and \mathbf{p}_2 . The second quantization provides, because of the density matrix, a link between correlations and multiplicity distributions. The correlation function is given by the ratio of the two-particle distribution to the product of the single-particle distributions [14]:

$$C_2(p_1, p_2) = \frac{P_2(\mathbf{p}_1, \mathbf{p}_2)}{P_1(\mathbf{p}_1)P_1(\mathbf{p}_2)}. \quad (2.12)$$

The density matrix approach can also be interpreted in terms of a Wigner phase space density $S(x, p)$, often also called “emission function”, which is the Wigner transform of the source density matrix [15]. The one-particle distribution can be written in terms of the emission function,

$$P_1(\mathbf{p}) = \int d^4x S(x, p), \quad (2.13)$$

where the four-vector $p = (E_p, \mathbf{p})$ is evaluated on-shell, i.e. $E_p^2 = m^2 + \mathbf{p}^2$. The correlation function is given, using $\mathbf{q} = \mathbf{p}_1 - \mathbf{p}_2$ and $\mathbf{K} = (\mathbf{p}_1 + \mathbf{p}_2)/2$ in terms of a four-dimensional Fourier transform of S as [16],

$$C_2(\mathbf{q}, \mathbf{K}) = 1 + \frac{\left| \int d^4x S(x, K) e^{iq \cdot x} \right|^2}{\int d^4x S(x, K + \frac{1}{2}q) \int d^4x S(x, K - \frac{1}{2}q)}. \quad (2.14)$$

This expression is true only for fully incoherent sources. In general, the four-momentum K is off-shell. Within the heavy ion collision context, where this formalism was developed, it was shown in Ref.[13] that K_0 can be approximated by its on-shell equivalent $E_K = \sqrt{m^2 + \mathbf{K}^2}$. While it is unclear to what level of accuracy this approximation holds in the case of hadron-hadron collisions, this point shall not be pursued further here.

It was shown by [17, 18] that the integrals in the denominator of Eq. (2.14) can be approximated by those evaluated at the average momentum K , so that (2.14) becomes

$$C_2(\mathbf{q}, \mathbf{K}) \simeq 1 + \left| \frac{\int d^4x S(x, K) e^{iq \cdot x}}{\int d^4x S(x, K)} \right|^2 \quad (2.15)$$

This is also used to define the theoretical expectation value used within the emission function

formalism,

$$\langle \dots \rangle = \left| \frac{\int d^4x S(x, K) \dots}{\int d^4x S(x, K)} \right|^2. \quad (2.16)$$

2.2 Experimental determination of C_2

2.2.1 Relation to cross sections

As set out in Section 2.1.3 above, only inclusive cross sections are measured. These cross sections are given by the one- and two-particle density functions ρ_1 and ρ_2 respectively,

$$\rho_1(p) = \frac{1}{\sigma_{\text{tot}}} \frac{d\sigma_{\text{incl}}}{dp}, \quad \rho_2(p_1, p_2) = \frac{1}{\sigma_{\text{tot}}} \frac{d^2\sigma_{\text{incl}}}{dp_1 dp_2}, \quad (2.17)$$

where p is the four-momentum of one particle, p_1 and p_2 are the four-momenta of particles 1 and 2 respectively, σ_{tot} is the total hadronic interaction cross section and σ_{incl} is the inclusive cross section. Since all experimental measurements are on-shell and $d^4p_i = d^3\mathbf{p}_i/2E_i$, this can also be written in terms of the three-momenta

$$\rho_1(\mathbf{p}) = \frac{2E}{\sigma_{\text{tot}}} \frac{d^3\sigma_{\text{incl}}}{d^3\mathbf{p}},$$

$$\rho_2(\mathbf{p}_1, \mathbf{p}_2) = \frac{4E_1 E_2}{\sigma_{\text{tot}}} \frac{d^6\sigma_{\text{incl}}}{d^3\mathbf{p}_1 d^3\mathbf{p}_2}.$$

The two-particle correlation function C_2 is defined experimentally as the ratio

$$C_2(\mathbf{p}_1, \mathbf{p}_2) = \frac{\rho_2(\mathbf{p}_1, \mathbf{p}_2)}{\rho_1(\mathbf{p}_1)\rho_1(\mathbf{p}_2)}. \quad (2.18)$$

2.2.2 Binning and correlation integrals

The correlation function is a basic element when doing statistical analyses. To implement it experimentally is not so easy, because of the six-fold differential and insufficient statistics. This is dealt with in part by projecting down to a smaller set of variables, for example integrating out the \mathbf{K} -dependence. In addition, the differential cross section is coarse-grained by introducing binning. Bin boundaries are defined for a specific measurement quantity or variable for which the correlations need to be determined. The particles are then thrown into a specific bin according to the bin interval in which their measured value falls. Linear binning (equally spaced bins) or logarithmic binning (to zoom in on the smaller scale) can be used.

In Fig. 2.2 linear binning is illustrated with the one-dimensional variable p_x , the x -component of the momentum. (For the purposes of illustration, the other components are taken to be zero ($p_y = p_z = 0$) in this subsection.) The crosses indicate the particles for a specific event in the

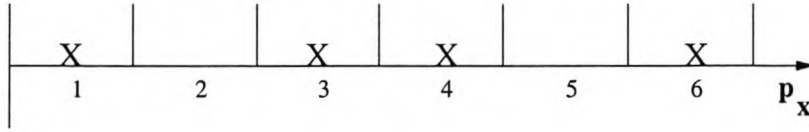


Figure 2.2: Example of simple binning. The crosses indicate the particles in a bin with a specific momentum p_x . Histogramming with the one-dimensional variable is done by just counting the particles in a specific bin.

different bins into which their momenta p_x fall. For each event, the number of particles in a specific bin is counted and added. This gives the experimental single-particle distribution for p_x .

For the two-particle density $\rho_2(p_{x1}, p_{x2})$, binning can be visualised by going into “Q-space” [19], which in this simple illustration is the two-dimensional space spanned by p_{x1} and p_{x2} . A point in Q-space then represents a pair of pions. A “bin” in Q-space is a square in the two-dimensional grid illustrated in Figure 2.3. If p_{x1} falls into bin 1 of Fig. 2.2 while p_{x2} falls into bin 3, the corresponding histogram count will be in bin (1,3) of Fig. 2.3. (Due to the symmetry of particles 1 and 2, this plot is symmetric about the diagonal, in other words, the pair bins (3,1) and (1,3) are identical.)

Measuring relative momentum $q_x = p_{x1} - p_{x2}$ is clearly not accurate in this scheme of simple binning. Since q_x is the distance between a particle pair point and the diagonal line $p_{x1} = p_{x2}$, measuring constant q_x therefore amounts to taking all squares which are at the same distance from the diagonal, as illustrated by the black squares in Fig. 2.3. This is not very pleasing,

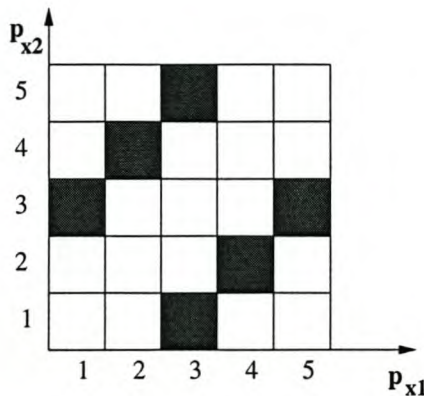


Figure 2.3: Two-dimensional grid for the determination of $\rho_2(p_{x1}, p_{x2})$. The shaded areas would be counted when we are interested in some specific q_x , which is the distance measured perpendicular to the diagonal $p_{x1} = p_{x2}$. This method is clearly unsatisfactory.

however, because of the uneven way in which these black squares sample a line of constant q_x : some pairs (p_{x1}, p_{x2}) will be counted, while others falling in adjacent “white” squares will not.

For this reason, experimentalists do a change of variables from (p_{1x}, p_{2x}) to q_x rather than binning p_{1x} and p_{2x} separately. Mathematically, this can be made exact by defining a per-event density function

$$\hat{\rho}_1(p_x) = \sum_i \delta(p_x - P_{xi}), \quad (2.19)$$

where P_{xi} is the x -component of the experimentally measured pion i 's momentum and the sum runs over all particles in the event. The two-particle per-event density function is

$$\hat{\rho}_2(p_{x1}, p_{x2}) = \sum_{i \neq j} \delta(p_{x1} - P_{xi}) \delta(p_{x2} - P_{xj}), \quad (2.20)$$

where the restriction $i \neq j$ explicitly excludes correlations of any particle with itself. The per-event histogram for pair variable q_x is found from

$$\hat{\rho}_2(q_x) = \int dp_{x1} dp_{x2} \hat{\rho}(p_{x1}, p_{x2}) \delta(q_x - |p_{x1} - p_{x2}|). \quad (2.21)$$

Inserting the above definitions yields a “correlation integral” [20, 21],

$$\hat{\rho}_2(q_x) = \sum_{i \neq j} \delta(q_x - |P_{xi} - P_{xj}|). \quad (2.22)$$

This looks the same as the one-dimensional case with p_x as the variable. The difference is however, that q_x already contains information on two particles and, of course, the sum runs over all pairs rather than just single particles.

Only at this step is binning implemented in q_x , given mathematically by

$$\hat{\xi}_2(m) = \int_{m\delta q_x - \delta q_x/2}^{m\delta q_x + \delta q_x/2} \hat{\rho}_2(q_x) dq_x, \quad (2.23)$$

where δq_x is the chosen bin width.

The effective “area” covered in Q -space by this correlation integral method is illustrated in Fig. 2.4. The change in variable to q and K is also indicated. The strip along the diagonal covers all possible pion pairs with a momentum difference smaller than the q_x given by the half-width of the strip. From this figure, it is also clear that we are integrating out K_x , which is the direction parallel to the diagonal.

The implementation of correlation integrals is an important improvement on simple binning. The integration domain is extended over the whole region, in that the domain is not just confined

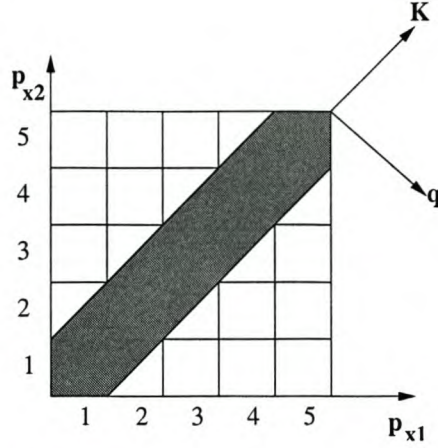


Figure 2.4: Correlations in terms of pair variables can be determined in two directions \mathbf{K} and \mathbf{q} . As BEC are important at the small relative momenta, the use of \mathbf{q} is more appropriate. The shaded area indicates the domain of integration for the correlation integral.

to the boxes in the grid. This method includes all pairs whose distance is less than a given length δ , including those that would have been in adjacent bins. By increasing the integration domain in this way, more particles can be counted and the statistics become better.

Looking at the two-dimensional case with q_l and q_t , the longitudinal and transverse components of \mathbf{q} (which will be explained in more detail later), the two-particle density becomes

$$\hat{\rho}_2(q_l, q_t) = \sum_{i \neq j} \delta(q_l - |P_{li} - P_{lj}|) \delta(q_t - |\mathbf{P}_{ti} - \mathbf{P}_{tj}|) \quad (2.24)$$

where \mathbf{P}_{ti} is the two-dimensional vector resulting from the projection of the three-momentum \mathbf{P}_i onto the transverse plane. The corresponding two-dimensional factorial moment results from the integration

$$\hat{\xi}_2(m, n) = \int_{m\delta q_t - \delta q_t/2}^{m\delta q_t + \delta q_t/2} dq_t \int_{n\delta q_l - \delta q_l/2}^{n\delta q_l + \delta q_l/2} dq_l \hat{\rho}_2(q_l, q_t). \quad (2.25)$$

All the above expressions are per-event. Corresponding sample averages are given by

$$\rho_1(x) = \langle \hat{\rho}_1(x) \rangle \quad (2.26)$$

$$\rho_2(x_1, x_2) = \langle \hat{\rho}_2(x_1, x_2) \rangle, \quad (2.27)$$

with x_1 and x_2 any variable that is used in the analysis, and correspondingly

$$\xi_2 = \langle \hat{\xi}_2 \rangle. \quad (2.28)$$

The above level of mathematical detail defining the correlation integral is clearly not needed for simple pair binning. Experimentalists often carry out a procedure equivalent to that of Fig. 2.4 without any reference to the mathematics. Its usefulness only emerges at higher orders, for example when considering triplets or quartets of particles. While the above formalism is hence not indispensable for two-particle correlation studies, it does provide a useful and accurate starting point. (It will also be used to derive event mixing below.)

The main advantage of correlation integrals is that, by enlarging the integration domain, better statistics are obtained and accuracy is improved. Correlation integrals have the general advantage of not introducing artificial binning as is the case with ordinary binning. There is a greater stability at small distances and it permits uniformly-spaced points in log-log plots. These advantages become increasingly important with higher orders of correlation.

2.2.3 Normalization

For normalization of the correlation function C_2 , a reference sample or background is needed without Bose-Einstein correlations. Ideally, the reference sample will contain all the information of the sample, missing out only on the Bose-Einstein correlations themselves. In practice, such a reference sample is not easily found but has to be explicitly constructed. Unlike-sign particle combinations like $\pi^\pm\pi^\mp$ were used for the reference sample at one stage, but these still exhibit strong correlations due to resonance decays (especially K^0 and ρ^0) and due to long-range charge correlations [22]. For this reason, the event-mixing technique was applied with good results [4, 11]. We will also make use of it in our experimental analysis.

The event-mixing technique starts with the product of single-particle distributions $\rho_1(x)$,

$$\rho_2^{norm}(x_1, x_2) = \rho_1(x_1)\rho_1(x_2)$$

where x is any one-particle variable of interest. Inserting the correlation integral prescription using Eqs. (2.19) and (2.26), we get

$$\rho_2^{norm}(x_1, x_2) = \left\langle \sum_i \delta(x_1 - X_i^a) \right\rangle_a \left\langle \sum_j \delta(x_2 - X_j^b) \right\rangle_b, \quad (2.29)$$

where the subscripts a, b on the event averages and on the particle coordinates X are needed to distinguish between the two averages involved. This can obviously be rearranged to

$$\rho_2^{norm}(x_1, x_2) = \left\langle \left\langle \sum_{i,j} \delta(x_1 - X_i^a) \delta(x_2 - X_j^b) \right\rangle_b \right\rangle_a. \quad (2.30)$$

Integrating to a relative coordinate $q = |x_1 - x_2|$ as above then results in

$$\begin{aligned} \rho_2^{norm}(q) &= \int dx_1 dx_2 \rho_2^{norm}(x_1, x_2) \delta(q - |x_1 - x_2|) \\ &= \left\langle \left\langle \sum_{i,j} \delta(q - |X_i^a - X_i^b|) \right\rangle \right\rangle_b \left. \right\rangle_a \end{aligned} \quad (2.31)$$

which shows that particles from different events a and b , with coordinates X_i^a and X_i^b are used to construct the normalization as if they belonged to the same event. Event mixing is therefore a natural and direct consequence of using the correlation integral formalism.

In theoretical work, the reference case is usually assumed to correspond to a Poissonian normalization, where the reference distribution factorizes into two single-particle distributions, as indicated in the denominator of Eq. (2.18), so for this case one would expect $C_2 = 1$. While this is not always true, and certainly not true for our data, the issues relating to the non-Poissonian overall distribution are side-stepped at this level of sophistication by renormalizing the various ξ_2 's to tend towards one at large q . In our analysis, this is accomplished by means of an overall multiplicative prefactor in the parametrizations.

2.3 Variables and LCMS

We saw how the study of Bose-Einstein correlations brought new developments in the theory as well as in experiments. Depending on the underlying physics involved some variables will be useful and others not; also different “good” variables will show up different aspects of the physics. Here we briefly survey the variables that have been in use, and discuss their relative merits and demerits.

2.3.1 One-dimensional variables

One-dimensional variables were formerly used because of the poor statistics that were available at the time. The rapidity y is defined as

$$y = \frac{1}{2} \ln \left(\frac{E + p_l}{E - p_l} \right), \quad (2.32)$$

where E is the energy and p_l is the component of the momentum \mathbf{p} in the direction of the beam axis as shown in Fig. 2.5. The rapidity is popular because it is additive under Lorentz transformations in the longitudinal direction. Another reason for using y is because of the plateau in $d\sigma/dy$ in the “central region” of small y .

The pseudorapidity η is defined as

$$\eta = -\ln \tan \frac{\theta}{2} = \frac{1}{2} \ln \left(\frac{p + p_l}{p - p_l} \right), \quad (2.33)$$

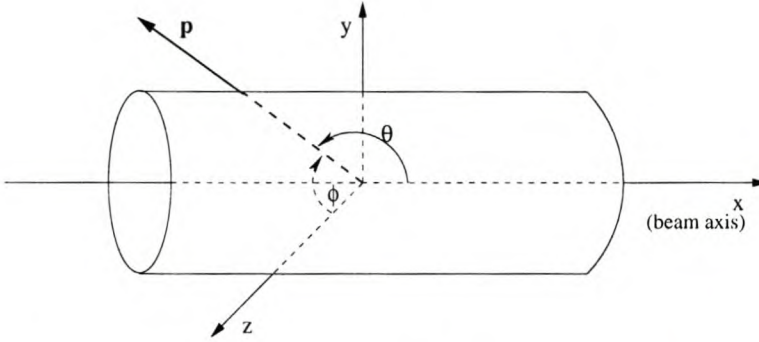


Figure 2.5: The momentum vector \mathbf{p} with θ and the polar angle and the azimuthal angle ϕ in the transverse plane perpendicular to the beam axis.

where $p = |\mathbf{p}|$ and θ is the polar angle between the momentum \mathbf{p} and the beam axis (see Fig. 2.5). The pseudorapidity is generally a good approximation for y , and does not need the mass of the detected particle to be calculated. UA1 used mainly η instead of y .

The azimuthal angle ϕ lies in the transverse plane and is defined as

$$\phi = \arctan\left(\frac{p_y}{p_z}\right), \quad (2.34)$$

where p_y and p_z are the transverse components of the momentum. The azimuthal angle is invariant under longitudinal Lorentz transformation, since it is purely in the transverse plane. This variable became interesting recently when azimuthal asymmetries were studied [23].

A very interesting variable is the four-momentum difference

$$Q^\mu = p_1^\mu - p_2^\mu, \quad (2.35)$$

with $p_i^\mu = (E_i, \mathbf{p}_i)$ with $i = 1, 2$ the four-momentum of a particle. Analyses in Q have often been done in terms of the squared four-momentum difference:

$$Q^2 = -(p_1 - p_2)^2 = (\mathbf{p}_1 - \mathbf{p}_2)^2 - (E_1 - E_2)^2. \quad (2.36)$$

There are a number of reasons why the four-momentum difference played such an important role as a variable in the Bose-Einstein correlation analyses. Firstly, it is Lorentz-invariant and hence yields the same results in any reference frame. Secondly, it is one-dimensional and thereby simplifies the correlation function which would be six-dimensional if \mathbf{p}_1 and \mathbf{p}_2 were used. It also yields better statistics for the same reason, even while being sensitive to three-dimensional

characteristics of the pair's momenta. This can be seen from the relation [9, 24]

$$Q^2 = 2 [m_{\perp 1} m_{\perp 2} \cosh(y_1 - y_2) - p_{t1} p_{t2} \cos(\phi_1 - \phi_2) - m^2] \quad (2.37)$$

(where $m_{\perp} = \sqrt{p_t^2 + m^2}$) which is small only when differences in all three directions, i.e. rapidity, azimuthal angle and transverse momentum p_t , are small.

In the third place, Q^2 is related to the two-particle invariant mass $M^2 = (p_1 + p_2)^2$ by

$$Q^2 = M^2 - 4m^2,$$

for equal masses $m_1 = m_2 = m$. Resonances are clearly revealed as bumps in the correlation function when plotted against Q^2 , and hence their influence can be separated from other effects if so desired. Fourthly, as correlation integrals allow to choose differences of phase space variables between particles, the Q^2 variable as a relative coordinate was very handy, in that it could be used as a distance in defining the correlations between the particles. For higher order correlations this simplifies the calculations a lot [25, 26, 27], not to mention their measurement [28, 9, 29].

In Ref. [6] it was also shown that if the pion sources were regarded as pointlike, the correlation function only depended on the relative four-momentum.

Nevertheless, the four-momentum difference has been neglected especially in the heavy-ion community, because most theoretical work is based on three-momenta so that Q^2 is regarded as an inappropriate projection of the higher-dimensional correlation function.

2.3.2 Three-momentum

To extract as much as possible information from Bose-Einstein correlations, the three momentum \mathbf{p} of the particle should be used. Hence, in principle a six-dimensional correlation function is needed for a full description of the correlations between two particles if their momenta \mathbf{p}_1 and \mathbf{p}_2 are considered. It is difficult to work and visualize in six dimensions, quite apart from the large statistics needed to make meaningful assertions. The theory as presented above seems to prefer relative coordinates like the momentum difference

$$\mathbf{q} = \mathbf{p}_1 - \mathbf{p}_2 \quad (2.38)$$

and the average of the pair momentum

$$\mathbf{K} = \frac{1}{2}(\mathbf{p}_1 + \mathbf{p}_2) \quad (2.39)$$

as the variables for the correlation function. These two variables \mathbf{q} and \mathbf{K} also popped up as natural variables in calculating the correlations when final state distortions were considered [14].

In analyses with the Wigner source function $S(x, K)$ (Section 2.1.3), the expressions for the correlation function simplified a lot when using \mathbf{q} and \mathbf{K} [30].

If we only take the momentum difference into account, the dimensionality of the correlation function between two particles immediately reduces to three. Due to limited statistics, UA1 has in general access only to relative three-momenta and must necessarily integrate out \mathbf{K} .

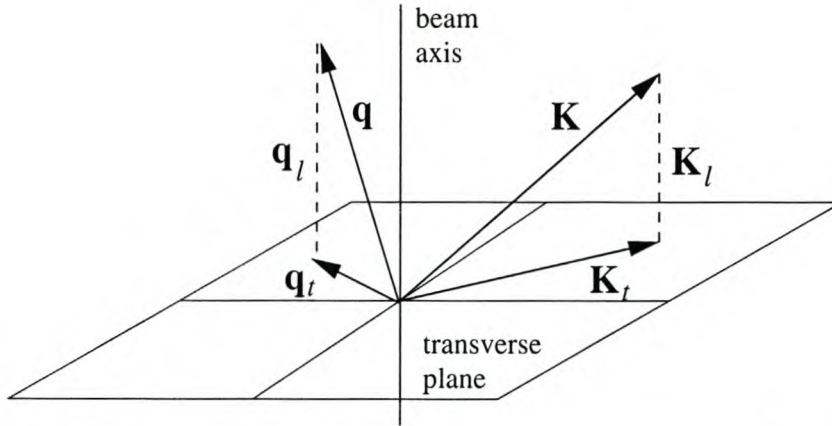


Figure 2.6: The momentum difference \mathbf{q} and the pair momentum \mathbf{K} with their various components in the longitudinal and transverse directions.

2.3.3 Transverse and longitudinal components

By selecting subsamples with only restricted regions of the directions of \mathbf{q} , or to study the two-particle correlation function for different components of \mathbf{q} , it is possible to get information on the structure of the particle source in different directions. This allows one not only to estimate the spatial size of the emitting source, but also its shape.

To study transverse and longitudinal Bose-Einstein correlations, the momentum difference of the pair of pions is resolved into two components, transverse \mathbf{q}_t and longitudinal \mathbf{q}_l as indicated in Fig. 2.6. The transverse component \mathbf{q}_t lies in the plane perpendicular to the beam direction and can be resolved into further components: q_s (sidewards) and q_o (outwards), as shown in Fig. 2.7. By convention, q_o is in the direction of the transverse of the pair momentum \mathbf{K}_t , while q_s is perpendicular to both q_o and q_l . In our analysis we restrict ourselves to the magnitude of \mathbf{q}_t given by

$$|\mathbf{q}_t| = q_t = \sqrt{q_s^2 + q_o^2}. \quad (2.40)$$

The longitudinal component q_l is in the beam direction and defined as the difference in the

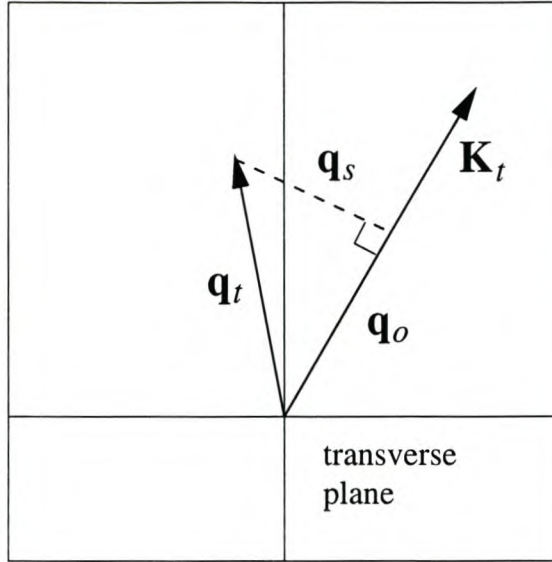


Figure 2.7: The components of the momentum difference \mathbf{q}_t in the transverse plane. The direction of \mathbf{K}_t defines the outward component q_o , and q_s is perpendicular to it.

longitudinal components of the momenta of the two particles:

$$q_l = p_{l_2} - p_{l_1}. \quad (2.41)$$

The longitudinal and transverse components of the vector \mathbf{q} show a noticeable difference in their correlation distributions. This is, of course, to be expected since the colliding proton and antiproton enforce a very strong directionality in the underlying physics.

In the longitudinally comoving system explained below, the component q_l reflects only the spatial difference of the two pions emitted, while q_t depends on the difference in emission time as well.

2.3.4 The longitudinal center-of-mass system

Since three-momenta are not Lorentz-invariant, the choice of reference frame in which the correlations are measured is very important in order to extract the relevant source parameters. Use of different reference frames that can be used for the components of the \mathbf{q} will alter the results as well as the dependence of the parameters on the source dimensions. In experimental studies, the parameters of the source are generally determined in either the lab frame or the center-of-mass frame of the reaction under study. In the case of a collider experiment like UA1, the lab system is, of course, also the overall center of mass system.

The longitudinal center-of-mass system (LCMS) [31], is defined as the system in which the

2. THE BOSE-EINSTEIN EFFECT

sum of the two particles' momenta in the longitudinal direction should be zero

$$2K_l = p_{l1} + p_{l2} = 0 \quad (2.42)$$

for every pair considered in the analysis. This implies that the sum of the momenta lies completely in the transverse plane (i.e. $\mathbf{K} = \mathbf{K}_t$), see Fig. 2.8. The LCMS hence involves a longitudinal Lorentz transformation, which leaves the transverse component of the momentum difference, q_t unchanged, but changes the longitudinal component q_l .

The LCMS variables are given in terms of the lab system by

$$\begin{aligned} p' &= \gamma(p - \beta E) \\ E' &= \gamma(E - \beta p), \end{aligned} \quad (2.43)$$

where p is the momentum, E the energy of the particle while β is the velocity of the boost and $\gamma = 1/\sqrt{1 - \beta^2}$. Decomposing the three momentum \mathbf{p} into a component parallel to β and one perpendicular to β yields: $\mathbf{p}' = p'_l + p'_t$. If only p_l transforms, then

$$\begin{aligned} p'_l &= \gamma_L(p_l - \beta_L E) \\ p'_t &= p_t \\ E' &= \gamma_L(E - \beta_L p_l). \end{aligned} \quad (2.44)$$

Using Eq. (2.42), leads to

$$\beta_L = \frac{p_{l1} + p_{l2}}{E_1 + E_2},$$

which is as expected, because $\beta_L = (2K_l/E)$ with $2K_l$ the total pair longitudinal momentum and $E = E_1 + E_2$ the total energy for the system. The γ -factor is then given by:

$$\gamma_L = \frac{E_1 + E_2}{\sqrt{(E_1 + E_2)^2 - (p_{l1} + p_{l2})^2}}.$$

Inserting γ_L into Eq. (2.44) gives, as it should,

$$p'_{l1} = \frac{E_2 p_{l1} - E_1 p_{l2}}{\sqrt{(E_1 + E_2)^2 - (p_{l1} + p_{l2})^2}} = -p'_{l2}. \quad (2.45)$$

The longitudinal momentum difference in the LCMS is then given by

$$q'_l = |p'_{l1} - p'_{l2}| = 2|p'_{l1}|. \quad (2.46)$$

This system is useful to obtain a clear interpretation of the observed difference between transverse and longitudinal correlation radii, when measuring the shape of the source, using Bose-Einstein correlations. LCMS is also sometimes referred to as the Longitudinal CoMoving System.

It must be emphasized that the LCMS is a transformation which is different from pair to pair. This is clear from the definition of β_L , which is clearly not a constant boost but pair-dependent. It is thus impossible to speak of an entire event in the LCMS except in the sense that every pion pair has been transformed separately to the LCMS.

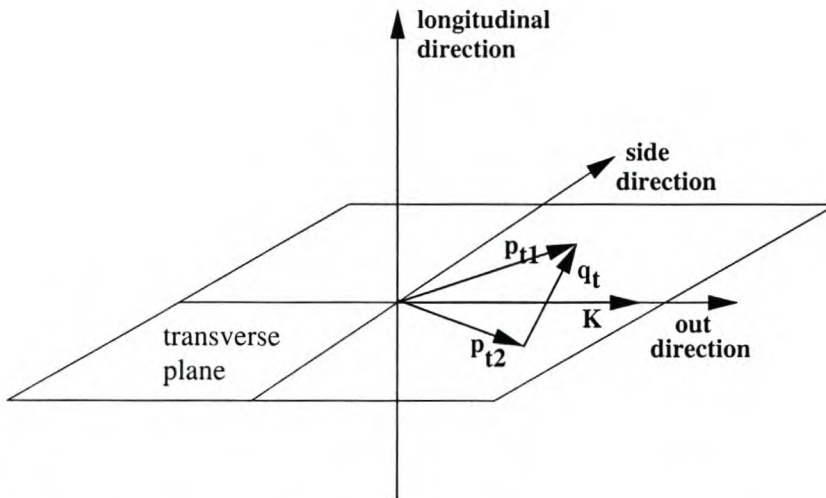


Figure 2.8: The Longitudinal Center of Mass System with \mathbf{K} in the transverse plane and showing the transverse relative momentum vector \mathbf{q}_t .

2.4 Parametrizations

To compare experimental results with a specific parametrization, the same components of the parametrization need to be used in calculating the correlation function. Meaningful interpretations of the radii can only be extracted from a specific parametrization if the same components of the momentum difference are used in the calculation of the correlations in the data.

The parametrization that you use, or that a given theorist proposes, determines the choice of variables, and specifically the choice of the components of the momentum difference \mathbf{q} . From the uncertainty relations, a given momentum difference (whether of the three- or four-momentum type) corresponds to $1/R$, where R is related to the corresponding spatial dimension of the source. If the correlation function is parametrized in the different components corresponding to the different directions of the momentum difference, the source dimensions (also referred to as the HBT radii) in different directions can be extracted. Likewise, the energy difference $q_0 = E_1 - E_2$

corresponds to $1/\tau$ where τ is the time of emission of pions from the source.

Experimental results in turn provide the required input and constraints for more sophisticated theoretical analysis.

Most parametrizations have a Gaussian form since they simplify the calculations a lot, and also have the advantage that if the source distribution function is Gaussian, the Fourier transform will also be Gaussian; see Section 2.1.2.

It is fortunately not necessary to choose exclusively one parametrization over others. Different parametrizations can be used to test the behaviour of experimental data in different ways.

2.4.1 Parametrizations in terms of four-momentum

The Gaussian parametrization with the four-momentum difference as variable,

$$C_2(Q^2) = 1 + \lambda e^{-R^2 Q^2}, \quad (2.47)$$

was used to study the Bose-Einstein correlations at small scale. The new parameter λ was introduced by experimentalists [32] since their data did not tend to a value of 2 for $Q^2 \rightarrow 0$ as the above parametrization would require if λ was absent. The conventional theoretical explanation for this parameter centres on the amount of coherence between pions: completely “chaotic” pions (those with random relative phases) would yield $\lambda = 1$, while coherent pions (with fixed relative phases) yield $\lambda = 0$.

Both NA22 and UA1 have found that the Gaussian parametrization in Q^2 could not fit their data [28, 29] although earlier results appeared to be compatible [33]. Exponential functions were implemented to better the results. Simple exponentials like

$$C_2(Q = \sqrt{Q^2}) = 1 + \lambda e^{-rQ}$$

fitted the data well and good fits were obtained when the Gaussian form was replaced by an exponential form [9]. Later it was found that by increasing the dimension of the analyses by going to three-momenta, the Gaussian parametrization gave a better result [34].

2.4.2 Cartesian parametrization

The Cartesian parametrization is based on the components of the relative three-momentum \mathbf{q} in the out-side-long coordinate system [35, 36], namely q_o (out), q_s (side) and q_l (long) as set out in Section 2.3.3. The out axis is defined by the transverse component of the pair momentum $\mathbf{K}_t = \mathbf{p}_{t_1} + \mathbf{p}_{t_2}$. The cross product of the longitudinal and out directions determines the direction of the side axis which is perpendicular to the other two (see Fig. 2.8).

For azimuthally, but not necessarily spherically symmetric sources and asymmetric sources,

2. THE BOSE-EINSTEIN EFFECT

a Gaussian source shape is generally assumed,

$$C_2(q_l, q_o, q_s) = 1 + \lambda e^{-r_l^2 q_l^2 - r_o^2 q_o^2 - r_s^2 q_s^2 - 2q_o q_l r_{ol}^2}, \quad (2.48)$$

where the “out-long” cross term $-2q_o q_l r_{ol}^2$ has been included, as it has been shown in Ref.[16] that its inclusion reveals more information about the source, while also increasing the accuracy of the other fitted radii. Due to the symmetries of the source in the transverse plane, the other cross terms (“out-side” and “side-long”) vanish.

The four fitting parameters, namely, r_l, r_o, r_s and r_{ol} , are also referred to as the HBT radii. The experimentally determined radii relate to the theoretical expectation values of the source distribution widths as follows [37]:

$$r_s^2 = \langle y^2 \rangle \quad (2.49)$$

$$r_o^2 = \langle (x - \beta_t t)^2 \rangle \quad (2.50)$$

$$r_l^2 = \langle (z - \beta_l t)^2 \rangle \quad (2.51)$$

$$r_{ol}^2 = \langle (x - \beta_t t)(z - \beta_l t) \rangle, \quad (2.52)$$

where y corresponds to the source size in the side direction, x in the out direction and z to the longitudinal direction, while β_t and β_l are the pion pair velocities in the transverse and longitudinal directions respectively.

These expressions have the form of variances of the Gaussian distribution of the source, as seen in the laboratory frame. The radii are interpreted as lengths of homogeneity [16, 18], i.e. the average distance over which pion pair momenta overlap to a significant degree to allow for quantum mechanical interference effects. For a static source, these lengths are equal to the source’s geometric size in the various directions.

The interpretation of the HBT radii from the Cartesian parametrization is that r_s measures the width of the emission region in the side direction, and r_o measures the corresponding width in the out direction together with a contribution from the emission duration t . The longitudinal component measures that region in the longitudinal direction where bosons with similar momenta may emerge from [38], also with a time component added to it.

Clearly, the measured radii mix spatial and temporal information on the source. From this parametrization it is not easy to extract accurately physical information such as emission duration. The LCMS, as defined in Section 2.3.4 was invented because, the longitudinal velocity is

zero ($\beta_l = 0$) in this frame and therefore the expressions for the radii simplify somewhat [37]:

$$r_s^2 = \langle y^2 \rangle \quad (2.53)$$

$$r_o^2 = \langle (x - \beta_t t)^2 \rangle \quad (2.54)$$

$$r_l^2 = \langle z^2 \rangle \quad (2.55)$$

$$r_{ol}^2 = \langle (x - \beta_t t)z \rangle. \quad (2.56)$$

The longitudinal radius, r_l is no longer dependent on the emission time but only on the longitudinal extension of the source. This leaves r_o as the only parameter to reveal information on the duration of the emission [13].

While the parameter of the cross term r_{ol} contains physical information about the emitting source, it has not in general been found to be significantly different from zero [13].

2.4.3 Transverse-longitudinal parametrization

A simplified version of the out-side-long system combines the two transverse directions into one, leaving only the components q_t and q_l of the momentum difference as defined in Section 2.3.3. The Gaussian parametrization for the correlation function in these components is given by:

$$C_2(q_t, q_l) = \gamma[1 + \lambda e^{-r_t^2 q_t^2 - r_l^2 q_l^2}]. \quad (2.57)$$

Since this is the parametrization used by our subsequent measurements, we have introduced an overall normalization factor γ , as is common in all such experiments. This parameter measures the deviation of the overall multiplicity distribution from a Poissonian, for which γ would be unity. Since it is well known that UA1 has a non-Poissonian overall multiplicity, the value of γ is of no further interest for us in this thesis.

Defining the direction of \mathbf{q}_t as \hat{w} (in the transverse plane), the transverse radius parameter can be expressed as:

$$r_t^2 = \langle (w - \beta_t t)^2 \rangle, \quad (2.58)$$

where w is the size of the source in the \hat{w} direction, $\beta_t = K_t/K^0$ and t is the characteristic time of source emission. As before, r_t and r_l are the HBT radii from which the source dimensions are determined. In the lab frame, both parameters will be dependent on the time as pointed out by Eqs. (2.51) and (2.58). In the LCMS time and space characteristics are contained in r_t , whereas r_l just measures the longitudinal dimension of the source, according to (2.55).

2.4.4 Yano-Koonin-Podgoretskii parametrization

In the Yano-Koonin-Podgoretskii (YKP) parametrization [39, 40, 41, 37, 30, 42, 13] the three independent components of the relative momentum that are used are the transverse component $q_t = \sqrt{q_o^2 + q_s^2}$, the longitudinal component q_l and the energy difference $q_0 = E_1 - E_2$ (not to be confused with the out component q_o). This parametrization assumes azimuthally symmetric, moving sources. The Gaussian ansatz for the correlation function in terms of these components is

$$C_2(q_t, q_l, q_0) = 1 + \lambda e^{-r_\perp^2 q_t^2 - r_l^2 (q_l^2 - q_0^2) - (r_0^2 + r_l^2) (q \cdot U(\mathbf{K}))^2}, \quad (2.59)$$

where $U(\mathbf{K})$ is a four-velocity with only a longitudinal spatial component

$$U(\mathbf{K}) = \gamma(\mathbf{K})(1, 0, 0, v(\mathbf{K})),$$

and $\gamma = (1 - v(\mathbf{K})^2)^{-1/2}$ and $v(\mathbf{K})$ the Yano-Koonin gamma factor and velocity which are closely related to the velocity of the source. The combination of the relative momentum $(q \cdot U(\mathbf{K}))^2$ is a scalar under longitudinal boosts and the radii fit parameters r_\perp, r_l and r_0 are longitudinally boost-invariant. This means that the parameters do not depend on the longitudinal velocity of the observer system in which the correlation function is measured. This is one of the most important properties of the YKP parametrization.

If we take the longitudinal velocity $v(\mathbf{K})$ to be zero, the parameters in terms of the variances are:

$$r_\perp^2 = \langle y^2 \rangle \quad (2.60)$$

$$r_l^2 = \langle (z - (\beta_l/\beta_\perp)x)^2 \rangle - (\beta_l/\beta_\perp)^2 \langle y^2 \rangle \quad (2.61)$$

$$r_0^2 = \langle (t - x/\beta_\perp)^2 \rangle - \langle y^2 \rangle / \beta_\perp^2. \quad (2.62)$$

The three HBT radii can be considered to measure the spatial and temporal lengths of homogeneity. In the YKP parametrization, r_\perp directly corresponds to transverse size. Only r_0 measures the emission duration (time) t , but has large uncertainties due to the limited region of q_0 that is available. The longitudinal parameter r_l has a combination of the spatial components and is dependent on the velocity in the transverse (β_\perp) and longitudinal (β_l) directions.

In the LCMS, the expressions for the radii simplify to

$$r_\perp^2 = \langle y^2 \rangle \quad (2.63)$$

$$r_l^2 = \langle z^2 \rangle \quad (2.64)$$

$$r_0^2 \approx \langle t^2 \rangle, \quad (2.65)$$

where the approximation is due to the dropping of small terms. Again, the transverse direction is considered Lorentz invariant, therefore the interpretation of r_{\perp} remains the same. The longitudinal parameter r_l simplifies to be only dependent on the source dimension in the longitudinal direction. The radius r_0 measures only the time during which particles are emitted from the source.

2.4.5 Parametrizations used by UA1

Here, we briefly summarize previous work done by UA1 in order to provide a context for our analysis. To study BEC, the variables q_t and q_l as proposed by Kopylov were implemented in Ref. [43]. The Kopylov q_t variable is the projection of \mathbf{q} onto the plane perpendicular to \mathbf{K} , while q_l is the projection of \mathbf{q} onto \mathbf{K} (in contrast to the Cartesian case, where the projections are made with respect to the beam axis). The correlations were determined by functions of q_t in the region of q_l . Two parametrizations were used. The first one was the Gaussian function

$$C(q_t) = \gamma[1 + \lambda e^{-\beta q_t^2}],$$

where the size of the source distribution is determined by β . The effective radius at which the source density is $1/e$ of its maximum value is $R = \hbar c \sqrt{\beta}$.

The second parametrization was the Bessel function

$$C(q_t) = \gamma[1 + 4\lambda J_1(q_t r)/(q_t r)^2].$$

Here, J_1 is the first order Bessel function and $R_b = r \hbar c$ is the radius of the spherical shell source. The Bessel function yielded a size of the interaction region about twice the size that was obtained with the Gaussian, consistent with the expansion of J_1 .

When studying higher order BEC in Ref. [9], it was observed that the measured correlation in Q^2 was steeper than expected. Functions of the Gaussian type $C(Q^2) = 1 + \lambda e^{-r^2 Q^2}$ or even more complicated expressions with quadratic terms in Q^2 did not fit the UA1 data so well, especially in the small phase space region. Simple exponential like $C(Q^2) = 1 + \lambda e^{-rQ}$ fitted the data well. This was taken to imply that Bose-Einstein correlations would dominate the intermittency effect in the small phase space regions.

In addition to the exponential mentioned above, UA1 data were also fitted with the following power-law functions in Ref. [29]:

$$\begin{aligned} f(Q^2) &= a + bQ^{-\phi} \\ f(Q^2) &= a' + b'e^{-rQ} \end{aligned}$$

as well as theoretically-determined extensions of these for third-order cumulants. The best

agreement with the data at small Q^2 was obtained by the power law. A power law in the correlation function implied strong fluctuations of the size of the interaction region [44]. There was also a possibility that the interaction region could be a self-similar fractal, extending over a large volume of about 6 fm.

In this thesis, we want to determine the source dimensions r_l and r_t in the transverse and longitudinal directions. To do this, we will use the two-dimensional Gaussian function with the transverse and longitudinal components of the momentum difference as the theoretical parametrization, as explained in Section 2.4.3. This is done in part because we do not have enough statistics for the three-dimensional case. Hopefully in the near future we will have better statistics available which will allow us to do the three-dimensional study with the components q_l, q_o and q_s for UA1 data.

CHAPTER 3 THE EXPERIMENT

The UA1 experiment is one of the few hadron-hadron experiments at high energies. Although the UA1 collaboration was dissolved around 1990, a small group carried on with data analysis. Together with “sister experiment” NA22, it has provided valuable results in the years since.

An outline of the experimental set-up and data acquisition will be given below.

3.1 The UA1 detector

3.1.1 General features

The experimental data used for the present analysis were obtained by the UA1 collaboration at the CERN SPS collider. The UA1 detector was optimized for the goal of obtaining experimental proof of the existence of charged intermediate vector bosons of the electroweak interaction, the W^+ and W^- . To do this, the following qualities were needed for the detector:

1. 4π coverage to detect the reaction products,
2. a capability to detect electrons by electromagnetic shower and muons by penetrating capability,
3. good visualization of charged tracks and accurate measurement of momenta,
4. measurement of the energy by calorimetry and detection of the missing energy and
5. a separation of leptons from hadrons.

The opened detector is shown in Fig. 3.1. It consists of a series of complementary detectors for track detection and calorimetry. A brief description of the main parts of the UA1 detector will be given here; for more details, see [45] and the references therein.

The electromagnetic calorimeters [46] completely surround the central detector. Independent measurements of the energy allows an energy profile which is used to identify the electrons and photons.

Outside the electromagnetic calorimeters is a magnetic coil which produces a uniform horizontal field of 0.7 Tesla in the region of the central detector. The field lines are oriented perpendicular to the beam-axis (x -axis) and parallel to the z -axis.

The hadron calorimeter [47] is behind the electromagnetic part of the calorimetry. It is formed of C-shaped modules and I-shaped modules, as indicated in Fig. 3.1. This calorimeter is used to measure hadronic energy.

3. THE EXPERIMENT

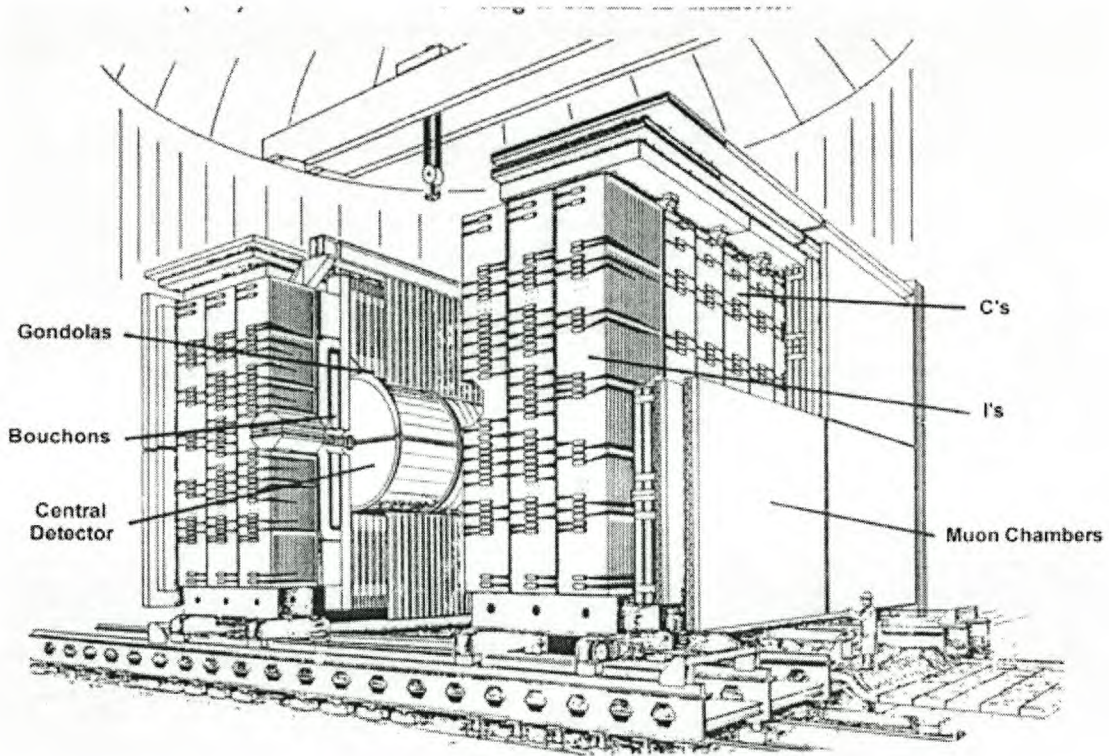


Figure 3.1: The UA1 detector with the central detector and surrounding calorimeters [45]. The size of the detector is calibrated by the experimentalist standing at the lower right.

To complement the electron identification, the above components are surrounded by muon chambers. Muons are identified through their ability to penetrate the entire central detector and so appearing as tracks in these large drift chamber arrays.

In the forward and backward regions there are also drift chambers, electromagnetic calorimeters and hadron calorimeters to detect particles with small scattering angles.

3.1.2 The Central Detector

The central detector (CD) is, as its name implies, the central part of the UA1 detector. It is also central in the sense that it is the most important part of the experiment and contains the interaction area. The CD is used to detect charged particles in the angular range $5^\circ < \theta < 175^\circ$, where θ , known as the polar angle, is the angle between the particle and the direction of the anti-proton beam (see Fig. 2.5). The momenta of the charged particles are measured by analysis of the deflection in the magnetic field.

3.1.2.1 Construction

The CD is a large cylindrical pictorial drift chamber. It extends over 25m^3 in volume, being 5.8m in length and 2.3m in diameter. The cylinder consists of six independent half-cylinder drift chambers. A schematic view of the arrangement is shown in Fig. 3.2. The chambers are filled

3. THE EXPERIMENT

with a gas mixture of 40% argon and 60% ethane at atmospheric pressure. The whole assembly is located in a dipole magnet generating a field of 0.7 Tesla as mentioned.

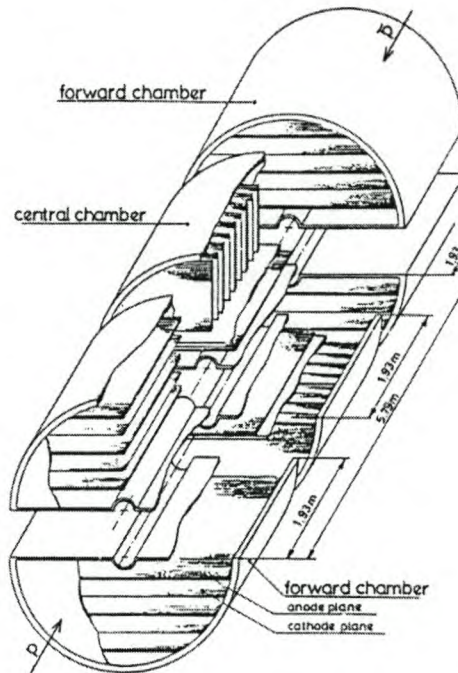


Figure 3.2: Schematic view of the central detector, with the four forward chambers having horizontal drift volumes and the two central chambers with vertical planes [45].

The wires in the drift chambers are organized into wire planes, which subdivide each of the six chambers into separate drift volumes. The drift volumes of the four forward chambers are horizontal and those of the central chambers are vertical. To fill the space between the beam pipe and the vertical wire planes of the central chambers, there are two extra volumes near the interaction region. The geometry has been chosen to give an approximately constant density of measurement points along the tracks over the total detector volume. The wire configuration of the chambers is chosen such that all the wires are parallel to the magnetic field.

The sense wires are surrounded by field-shaping wires. The sense wire ends are connected to preamplifiers mounted on the outside surface of the CD. From the preamplifiers, the pulses are digitized in the counting room. The wire positions are accurately known through accurate assembly.

3.1.2.2 Detecting charged hadrons

Protons and anti-protons, each coming in bunches of about 30cm in length, collide at the center of the apparatus. The interaction region is inside a stainless steel beam pipe. An assortment of charged and neutral hadrons are then formed by the interaction.

To detect a charged particle, soft electromagnetic interactions are used, which allow the

particle to pass through with almost no change in trajectory. Cherenkov radiation, energy loss (dE/dx) and transition radiation are such electromagnetic processes. Energy loss occurs when a charged particle passing through matter loses energy by electromagnetic interactions with atomic electrons, resulting in excitation and ionisation of these atoms. The expression for dE/dx represents the average energy loss per unit distance. The characteristic shape for the energy loss distribution, permits identification of the particle.

The charged particles that are formed by the collision or interaction, pass through the chamber and ionize the chamber gas. Free electrons are then created which drift in an uniform electric field towards the sense wires. Near the sense wires, the gradient of the electric field becomes large enough for the drift electrons to gain sufficient energy to ionize the gas and to initiate an avalanche. The charge collected on the sense wires from the avalanche produces a pulse which is measured and read out at both ends of the wire. The energy loss (dE/dx) is measured by the sum of the two pulses through a non-linear scale in order to increase the dynamic range.

The read-out system records continuously the information on the drift time, charge division and pulse height from both ends of each wire with fast analog to digital converters (FADCs). The drift time measurement combined with the known wire positions provides two precise coordinates of the track position in the plane perpendicular to the wires. The third coordinate is obtained by charge division, where the relative amount of charge seen at the two wire ends provides a measure of the position along the wire. The measured positions are known as the space points of the particle. On the average the trajectory of a charged particle is measured at over 100 space points.

The momenta of the charged particles are measured by analysis of the trajectory deflection in the magnetic field. The momentum accuracy is limited by systematic errors on the chamber alignment and by the diffusion of the drifting electrons. This results in a momentum uncertainty of $\Delta p/p^2 = 0.005(\text{GeV}/c)^{-1}$ for a 1m long track perpendicular to the magnetic field. To keep systematic errors well below the statistical measurement errors, careful construction, calibration and monitoring of the whole detector is required.

3.1.3 Data acquisition and reconstruction

The data acquisition system operates in separate stages [48]. This is a very powerful system which accommodates the high trigger rate and the large data volume of the central detector. The data acquisition system receives a start signal from a beam crossing. This is also the start for the drift chambers and the scintillation hodoscopes in the forward arms of the detector for selecting $p\bar{p}$ interactions. This “pre-trigger” is used either for minimum-bias data taking or as the start of the main trigger system [49]. The trigger system digitizes the data very rapidly. All electronic data is written to tape.

The conversion of the raw data into tracks is fully explained in [45], so I will give just a brief

outline. All tracks recorded in the CD are reconstructed first from the drift time measurements in the xy -plane. The dip angle λ with respect to this plane, as shown in Fig. 3.3, is determined from the charge division on the wires which are parallel to the magnetic field. The space points are used to construct segments of about three points on a line. From each segment, the radius of curvature, circle origin, segment position and length in helix circumference are stored. Also the start, middle and end point coordinates and master points are stored. This information is used in the global track reconstruction. The track segments are then combined by a global road method [45] to form longer tracks.

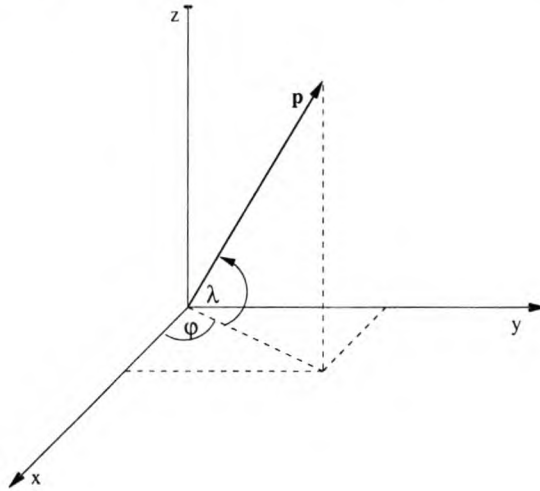


Figure 3.3: Coordinate axes for the detector measurements: momentum \mathbf{p} , dip angle λ and φ the angle in the xy -plane. The direction x corresponds to the beam axis.

After the track-fitting procedure, the tracks have to pass a geometrical fit. A helix is used for the parametrization of the particle trajectory. The projection of the helix parametrization onto the xy -plane is a circle and that along the field can be represented by a straight line. After the track has passed the geometrical fits, the ionisation loss (dE/dx) is calculated.

When the tracks are reconstructed and the parameters defined, the vertex is located. This is done by extrapolating every track back to the known beam line. The biggest cluster of points (crossings) is taken to correspond to the real vertex.

All reconstructed track pairs of same charge, similar momentum and with an opening angle $\leq 18^\circ$, have been analysed separately and the second piece of a split track has been removed. All pairs with like charge, an opening angle $\leq 1.4^\circ$ in the xy -plane and $\Delta\lambda < 2.5^\circ$ have been eliminated in order to avoid problems with the two-track resolution.

A further two track resolution test is performed in the CD for tracks of the same charge and momentum. The two tracks are separated if each track has at least a 30 cm track piece which is separated more than 15mm from the other in the xy -plane. With BEC being an essentially

two-particle measurement, biases such as those mentioned here, and their careful and proper treatment are very important.

The combined effect of variable pulse shape, the number of points and other quality requirements gives rise to variation of the acceptance as a function of particle rapidity y , azimuthal angle ϕ , charge and transverse momentum p_t . The detector acceptance also depends on the topology of the events studied. For minimum bias type data the azimuthal symmetry and rapidity plateau within a fixed p_t interval has been used.

The distribution of the track points in the $\phi - \eta$ -plane, where ϕ is the azimuthal angle and η is the pseudorapidity, is shown in Fig. 3.4. The worst acceptance areas are seen as empty regions in the plot. They are due to the geometrical effects of wire configuration and drift angle, as a certain length and number of points is required. The magnetic field in the z -direction is responsible for the bad acceptance areas.

Careful treatment of acceptances too, is even more important for correlation studies than for singly differential cross sections. Pair acceptances are for example, also more sensitive to event multiplicity than single particle acceptances.

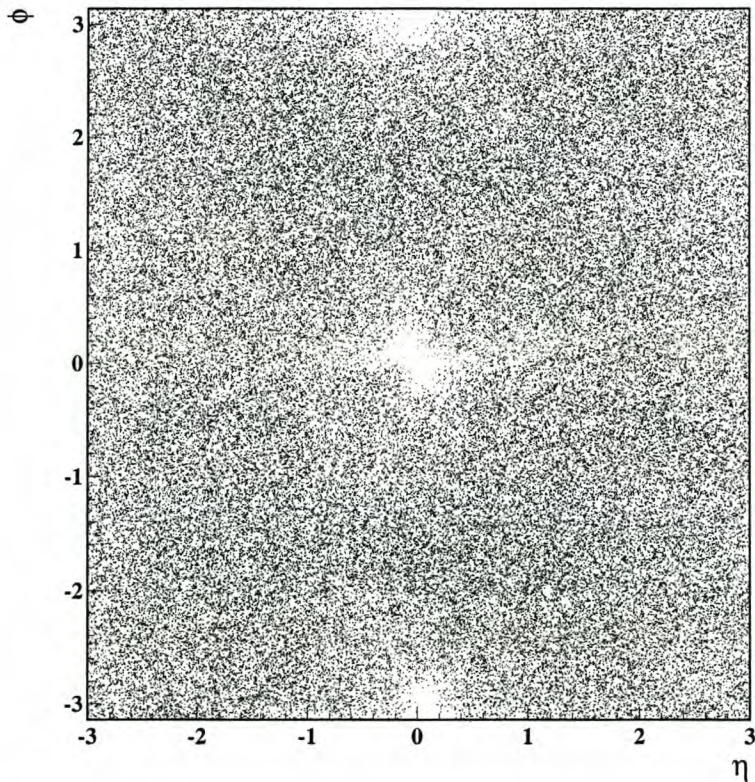


Figure 3.4: Scatter plot of all charged pions with azimuthal angle ϕ and pseudorapidity η (before cuts). Holes can clearly be seen which corresponds to the bad acceptance due to the magnetic field in the z -direction.

3. THE EXPERIMENT

3.2 Data sample and analysis

3.2.1 The sample and cuts

While the reduced NANO data set available for our analysis does contain particle identification information, this has not in general been used due to time constraints. The “pion” sample used therefore contains $\sim 15\%$ kaons. The data sample from the 1985 run used in our analysis consists of approximately 160000 non-single diffractive events at $\sqrt{s}=630\text{GeV}$. We placed no restriction on the multiplicity in the analysis. All data was taken using a minimum bias trigger. The information used was obtained from reconstructed trajectories measured by the UA1 central detector. Only charged tracks associated with the primary vertex and with transverse momentum of $p_t \geq 0.15\text{GeV}/c$ have been used. Pseudorapidity was restricted to the interval $\eta \in [-3, 3]$. The tracks had good measurement quality and the minimum length of the tracks was 30cm.

In the analysis, a specific variable gets chosen, together with the range/region of analysis. The track data was read from the file in the form of the detector coordinates $(\varphi, \lambda, 1/p)$ as shown in Fig. 3.3, and particle charge, from which the azimuthal angle ϕ , pseudorapidity η and momentum $|\mathbf{p}|$ were calculated. All other quantities follow as set out previously.

3.2.2 Correlation-specific cuts

Correlation analysis requires extra care also in the application of cuts at small relative pair momentum. The reason is, of course, that detectors experience all sorts of difficulties when two tracks are close to each other; in addition, this is precisely the kinematic region most important to determining correlation parameters. In the early days of “intermittency” analysis, for example, the existence of “ghosts” was found to have a major influence on experimental results [50]. Careful consideration of such effects was therefore imperative in this analysis also.

1. The **alpha cut** is a software cut which was first introduced after Neumeister found that in a plot of the number of pairs as a function of four-momentum difference Q^2 , there was a bump at small Q [51]. This bump was traced to the fact that a single track could sometimes be seen by the detector as a succession of pieces of tracks which the track fitting algorithm considered to be two tracks. After consultation with experimental collaborators [52] on how the resolution of the detector determined these ambiguities, the alpha cut was implemented in our analysis to get rid of this problem as follows:

If tracks are separated by more than 15mm then they can be resolved in the xy -plane. This means that there is no fixed minimum angle between the two tracks because resolution is distance-limited and not angle-limited; in other words, if two tracks have a small angle difference but their tracks do eventually separate by more than 15mm, then they can still be resolved. The alpha cut thus becomes distance limited and not angle limited.

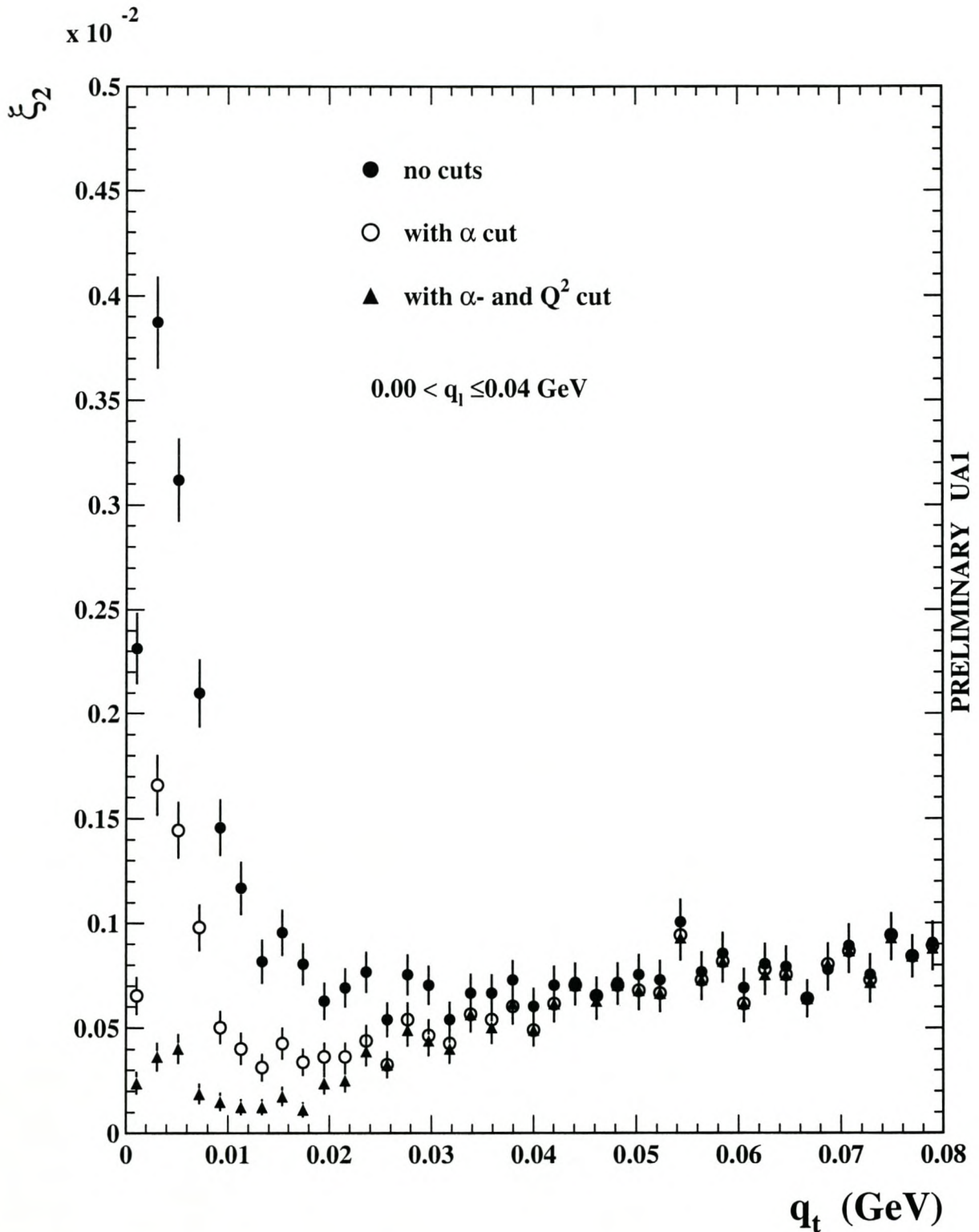


Figure 3.5: Plot of ξ_2 versus q_t showing the effect the alpha and Q^2 -cuts have in the small phase space region. The closed circles indicate the data points without any cuts applied. The open circles are after the alpha cut was implemented. The triangles indicate the effect after an additional cut Q^2 was applied.

2. The **four-momentum difference cut** that was originally put into the end of subroutine `isola2` of our analysis program was, strictly speaking, not a ghost cut but one which was designed to get rid of very small Q pairs, since it was thought that all pairs with $Q < 20$ MeV could necessarily not be resolved.

We found, however, that there were pairs which *did* have azimuthal angle differences larger than the minimum value $\Delta\phi$ or which have momentum differences larger than the momentum difference Δp , but which at the same time have a Q^2 smaller than the Q^2 -cut implemented in `isola2`. Since such pairs would exit the `isola2` routine before encountering the Q^2 -cut, they were not removed by the Q^2 cut at the end of the `isola2` routine. Such pairs would hence appear below the putative Q^2 cut even though logic would say that no such pairs could remain after `isola2`. In this sense, the Q^2 cut was softened to accommodate such pairs which were perfectly acceptable.

The following graphs show the effect the cuts have on the q_t - and q_l -variables with restriction to small intervals. The second moment ξ_2 is the count of the number of pairs in a specific bin. The slight change that occur at the larger values, is probably due to the fact that tracks, not pairs, are removed when cuts are implemented, and that such removed tracks are then not taken into account at higher Q also.

3. As can be seen from figure 3.4, the detector has bad acceptance areas around $\phi = 0^\circ, \pm 180^\circ$. An **azimuthal cut** was therefore implemented which cut away the ranges $-45^\circ \leq \phi \leq 45^\circ$ and $135^\circ \leq \phi \leq 225^\circ$. We used this “good azi cut” (and thereby sacrificed statistics) because the excellent acceptance in the remaining azimuthal region makes it unnecessary to make further corrections based on Monte Carlo simulation. As shown in Fig. 3.7 the acceptance loss is more or less constant between all azi and good azi. The acceptance of the tracks is multiplicity dependent, therefore the graph of good azimuth lies above that of all azimuth.

3.2.3 Normalization

For the normalization, the event mixing technique explained in Section 2.2.3 was used. The very long CPU time needed for performing the double event averages inherent in the event mixing technique were circumvented by constructing an “event ring”, i.e. a pool of events updated for every “numerator event” and taking randomly selected tracks from these pool events in the ring to make up the “fake events”. This procedure constitutes a sampling of the full normalization embodied in the double event average.

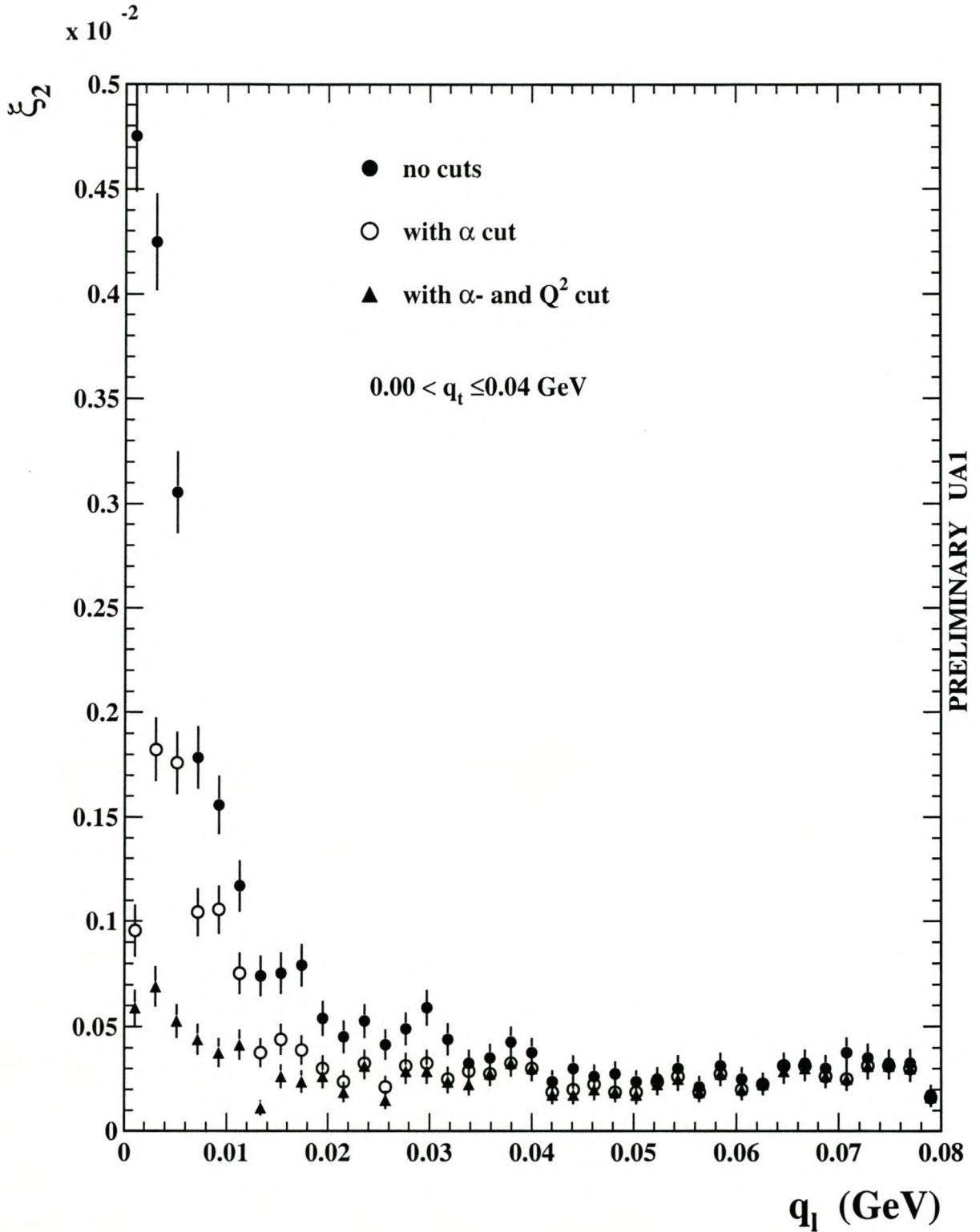


Figure 3.6: Plot of the unnormalized correlation ξ_2 versus q_1 , showing the effect the alpha and Q^2 -cuts have in the small phase space region. The closed circles indicate the data points when no cuts were applied, open circles those after the alpha cut was implemented. The triangles indicate the effect after an additional cut Q^2 was applied.

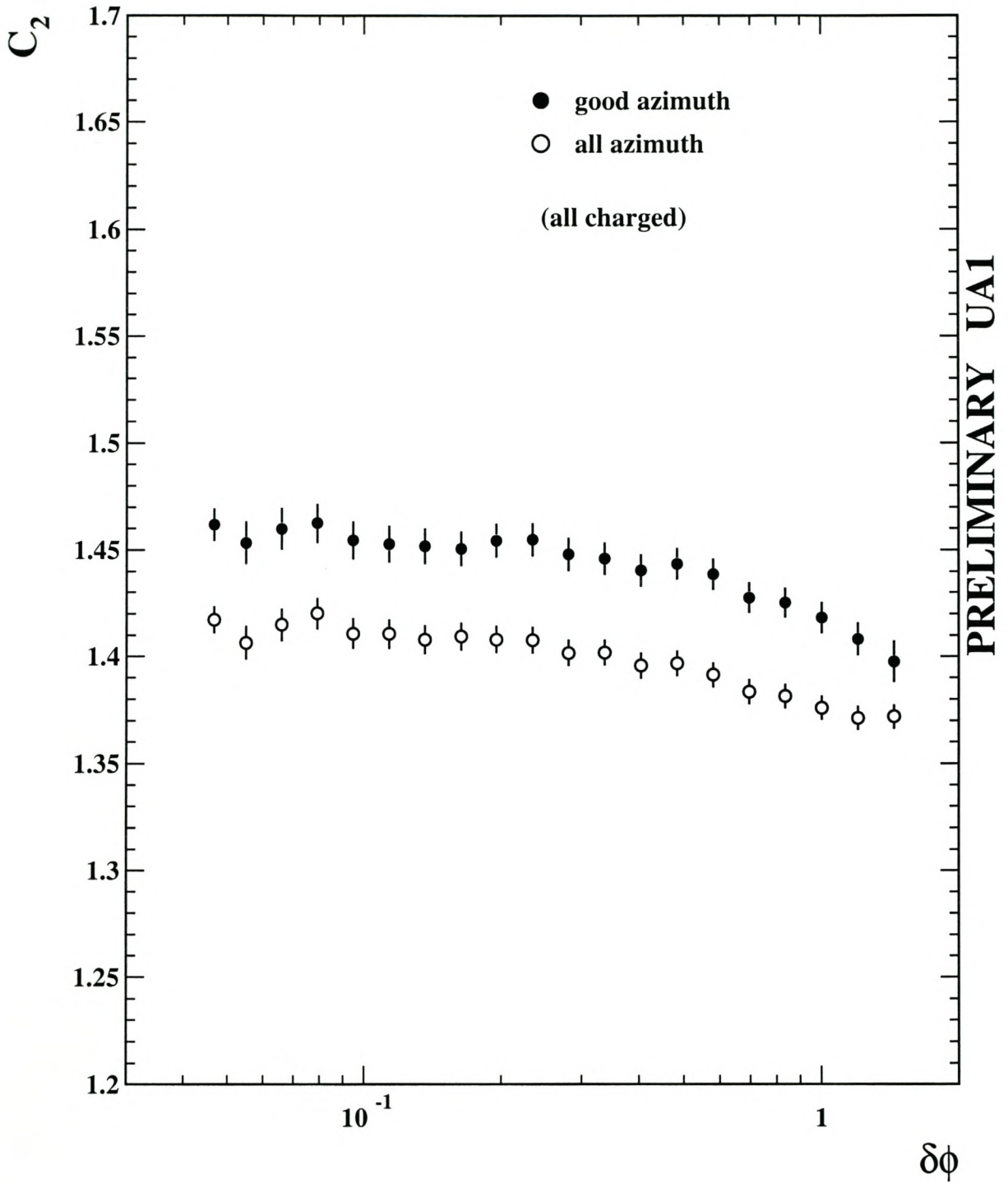


Figure 3.7: The correlations as a function of the azimuthal angle, displaying the difference between the all azimuth and the good azimuth regions and hence the effect of the azimuthal cut.

CHAPTER 4

RESULTS AND DISCUSSION

We now present results of our analyses, first in a variety of one-dimensional variables, followed by the two-dimensional (q_l, q_t) case.

These results were obtained for second-order correlations using software previously developed for the correlation integral. The program was modified to accommodate the new variables and techniques specific to these. Extensive use was also made of the HBOOK and PAW packages and other CERNLIB routines. Scatter plots, cuts and singly-differential cross sections were all repeated or extended as set out previously and checked against earlier UA1 results.

In the one-dimensional case, all-charged correlations were included for comparison; these include all possible charged pion combinations $(\pi^\pm\pi^\mp, \pi^+\pi^+, \pi^-\pi^-)$. For the like-sign analyses, carried out for both one- and two-dimensional cases, the negative-negative $(\pi^-\pi^-)$ and positive-positive $(\pi^+\pi^+)$ outputs were averaged according to

$$C_2^{ls} = \frac{1}{2} \left[\frac{\rho_2^{++}(x)}{\rho_1^+ \otimes \rho_1^+(x)} + \frac{\rho_2^{--}(x)}{\rho_1^- \otimes \rho_1^-(x)} \right], \quad (4.1)$$

where $\rho_2^{\pm\pm}$ is the measured two-particle density of positive-positive and negative-negative pion pairs respectively, and $\rho_1^\pm \otimes \rho_1^\pm$ is the normalization by event mixing as explained in Section 2.2.3. The variable x stands for any of the one- or two-dimensional variables used below. It is important to normalize the $++$ and $--$ cases separately as the UA1 acceptances for these differ by some 10 percent. Averaging over both instead of just using $(\pi^+\pi^+)$ or $(\pi^-\pi^-)$ doubled the statistics, making up in part for the loss of statistics due to the drastic azimuthal cut.

4.1 One-dimensional analysis

For the one-dimensional analysis, the correlation function C_2 was measured for the variables $\delta\eta$ (pseudorapidity), $\delta\phi$ (azimuthal angle), and Q^2 (four-momentum squared) as shown in Figs. 4.1, 4.2 and 4.3 respectively. Logarithmic binning was used here to zoom in on the smaller pair separations. Since most physical correlations are strongest at small relative momentum, such logarithmic binning reveals important structure which is invisible in the conventional linear binning.

The same tendencies for the various C_2 's as in former publications [51, 20] were observed. The rise in the azimuth ($\delta\phi$) is not so strong as with the pseudorapidity ($\delta\eta$): note the very different scales on the y -axes. This implies weak correlations in the azimuthal angle. At low Q^2 , a clear enhancement can be seen, again in agreement with previous work.

A comparison of Fig. 4.1 with Fig. 4.3 reveals why η has fallen out of favour while the four-

momentum continues to be interesting. Little structure can be seen in $C_2(\eta)$, for either like-sign or all-charged plots, while the behaviour of $C_2(Q^2)$ differs a lot for the two cases. Clearly, the projection of the six-dimensional physics onto η leaves little to be seen, while Q^2 remains sensitive to the physics of the six-dimensional phase space.

The plots show also that formerly popular all-charged plots are not so useful, since they also amount to an averaging over interesting information. This is clear when considering how the all-charged two-particle moment can be decomposed into the various charge combinations:

$$\rho_2^{\text{all charged}} = \rho_2^{++} + \rho_2^{--} + \rho_2^{+-} + \rho_2^{-+} \quad (4.2)$$

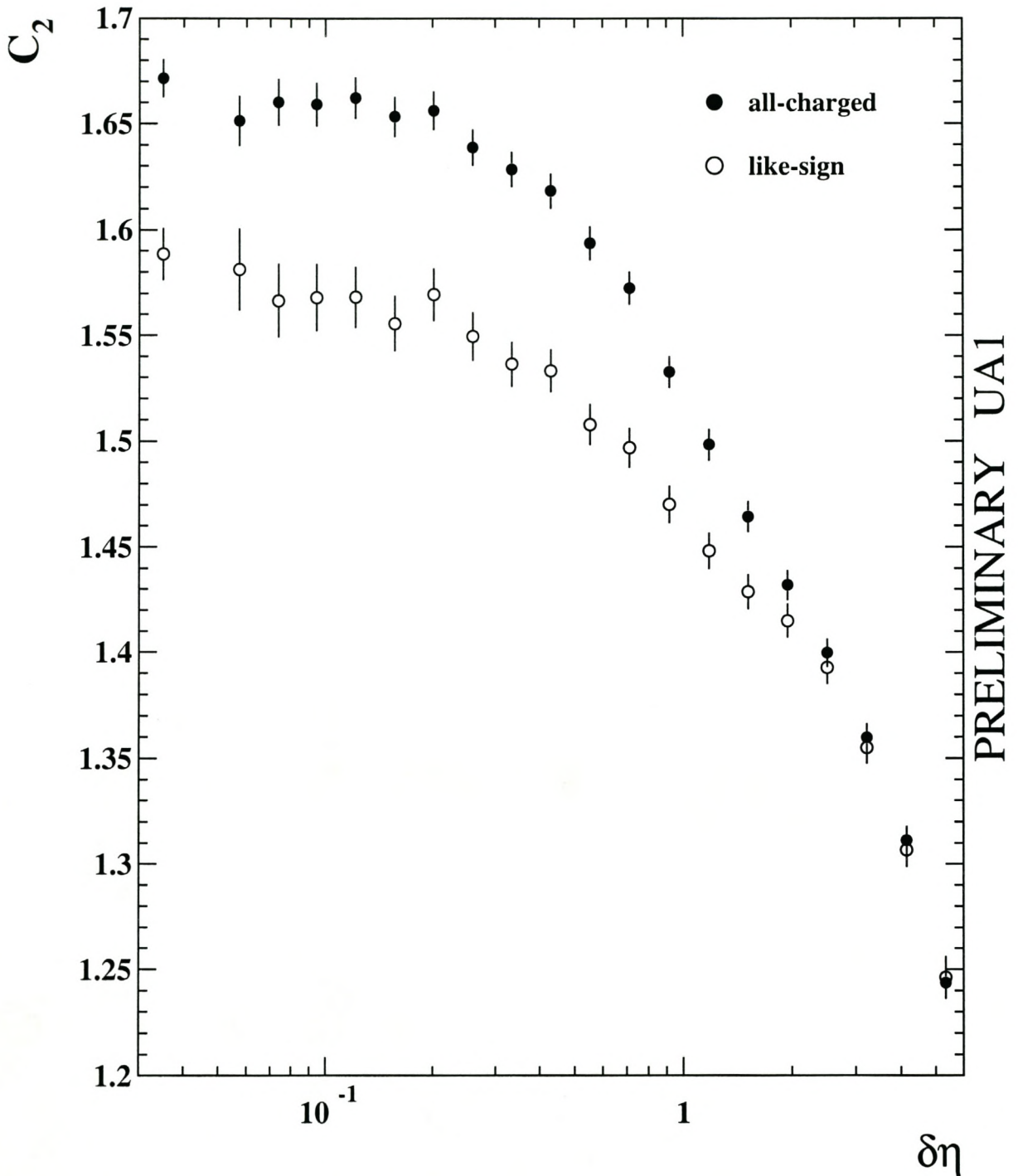
which, when normalized by the square of $\rho_1^{\text{all charged}} = \rho_1^+ + \rho_1^-$ shows how these different charge contributions are averaged out. Buschbeck and others [53] have previously analysed like-sign and unlike-sign UA1 correlations in some detail, showing that unlike-sign correlations remain approximately constant at small Q while like-sign rise steeply. The all-charged case presented here, being an average of the two, shows something of both these features.

Looking at the one-dimensional components of the three-momentum difference, $|\mathbf{q}_t| = q_t$ and $|\mathbf{q}_l| = q_l$ (discussed in Section 2.3.3), the same tendency, that is, a general rise in the correlations for smaller values of the abscissa, can be observed.

In the case of the q_t -variable shown in Fig. 4.4, a rise in the larger values (for $q_t > 600$ MeV) is observed as well. This is due to momentum conservation in the transverse direction. The cylindrical phase space causes a restriction in the transverse direction, where one is more likely to encounter a pair of pions both with large p_t but travelling in opposite directions than in the corresponding mixed events (see Sec. 2.2.3) for more details).

As for $C_2(q_t)$, the errors for $C_2(q_l)$ in Fig. 4.5 are large in the small bin region. This is due to insufficient statistics, or, in another terminology, the empty bin effect, which arises when the bin sizes become so small that the average multiplicity per bin becomes very small [54, 55]. The rise in the smaller bins, which is evident of BEC, is not so strong in the q_t - and q_l -variables as compared to the four-momentum difference squared (Q^2) in Fig. 4.3. It remains debatable whether this is an effect of projection only or a reflection of the more Gaussian nature of correlations in this variable.

When using linear binning for the q_l variable, again with no restriction on q_t , the rise becomes more pronounced in the smaller bins (Fig. 4.6), leading one to doubt the Gaussian nature of $C_2(q_l)$. The contrast between Figs. 4.5 and 4.6 reveals the pitfalls and prejudices embodied in viewing correlations in linear binning only: does the physics prefer a Gaussian shape (as the eye would suggest based on Fig.4.5) or something more exponential (as in Fig. 4.6)? This dilemma is resolved by simply looking at goodnesses of fit in mechanical fitting procedures: the χ^2 are based on very different numbers of small- and large- q_l data points in the two cases.

Figure 4.1: Plot of the correlation function C_2 versus $\delta\eta$ for all charged and like-sign particles.

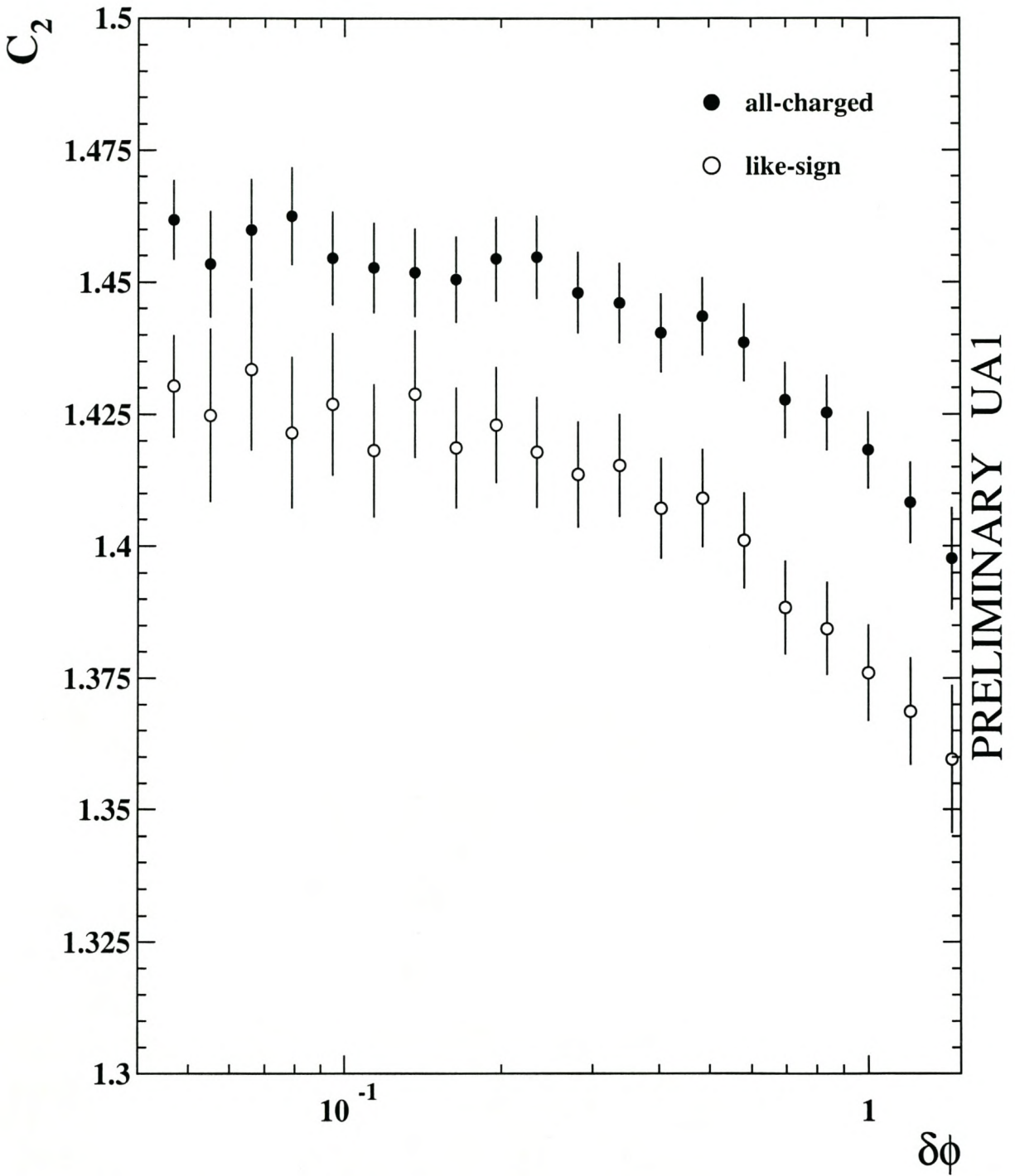


Figure 4.2: Plot of the correlation function C_2 versus $\delta\phi$ for all charged and like-sign particles. Note the different scale on the y-axis.

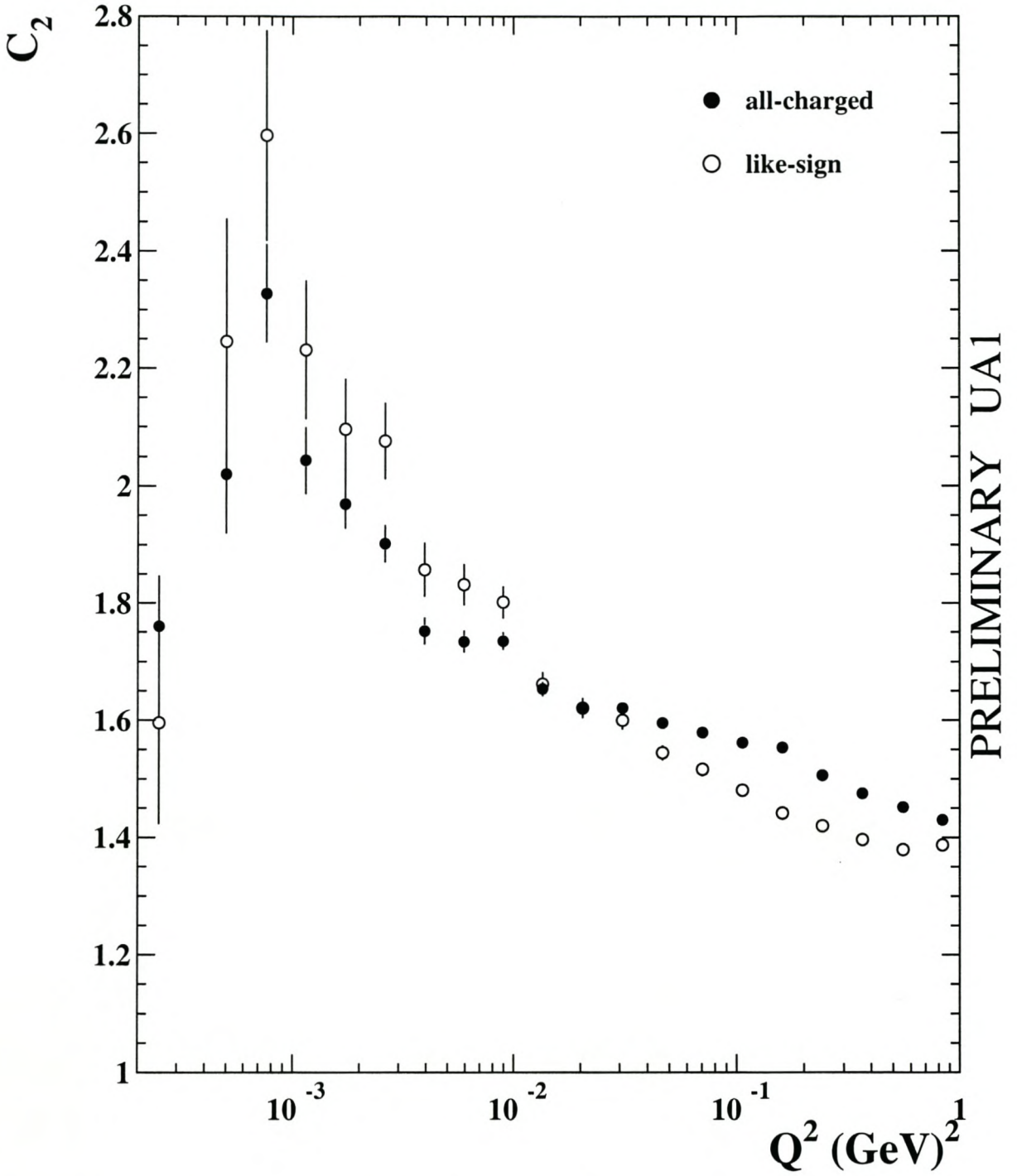


Figure 4.3: Plot of the correlation function C_2 versus Q^2 (four-momentum difference squared) for all charged and like-sign particles. The two leftmost points fall within the problem region discussed in Section 3.2, and hence cannot be taken seriously. The strong rise in like-sign was previously observed by UA1 [9].

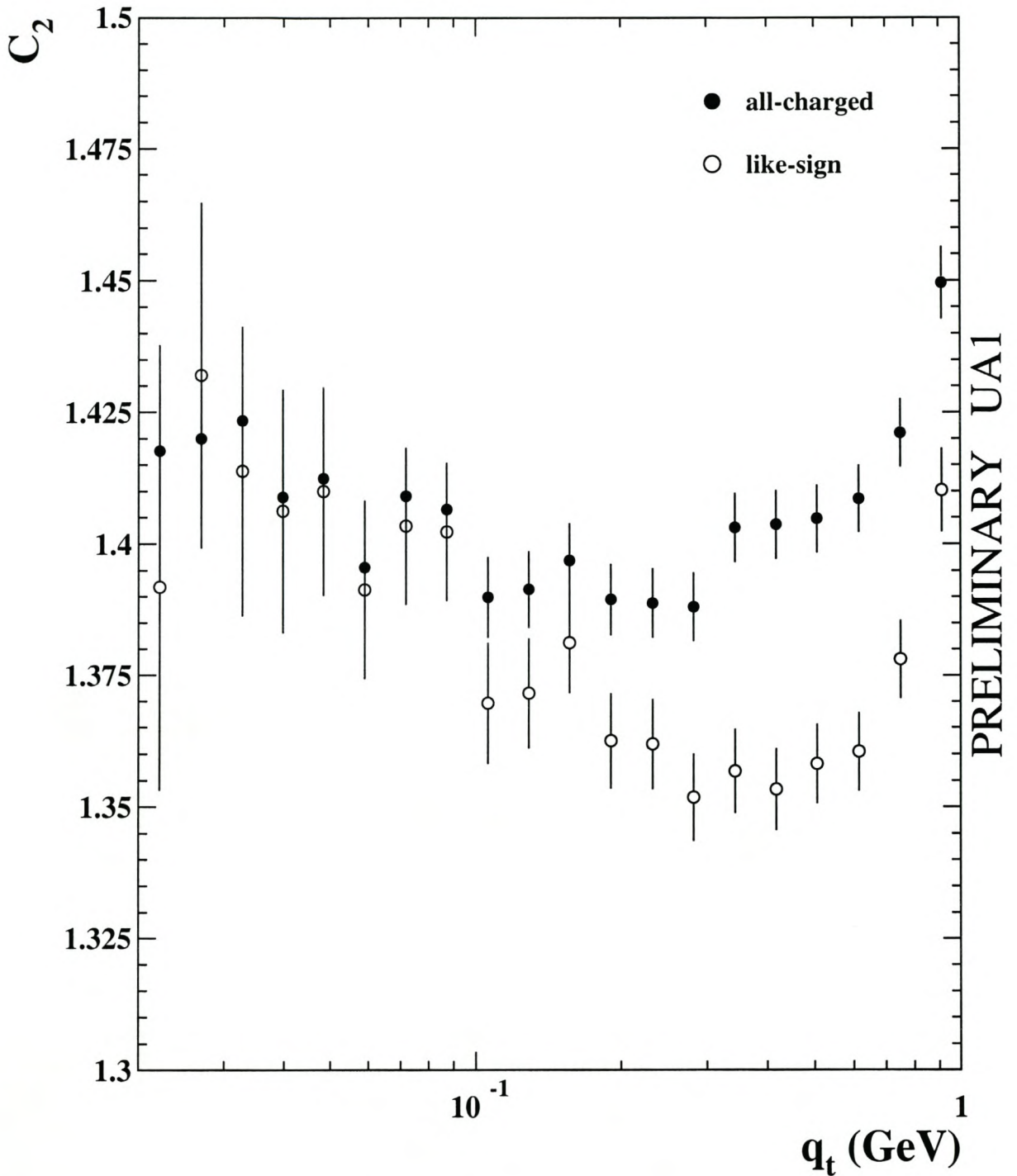


Figure 4.4: Plot of the correlation function C_2 versus q_t , the transverse component of the three-momentum difference, for all charged and like-sign particles. The rise at $q_t > 600$ MeV can be attributed to conservation of transverse momentum.

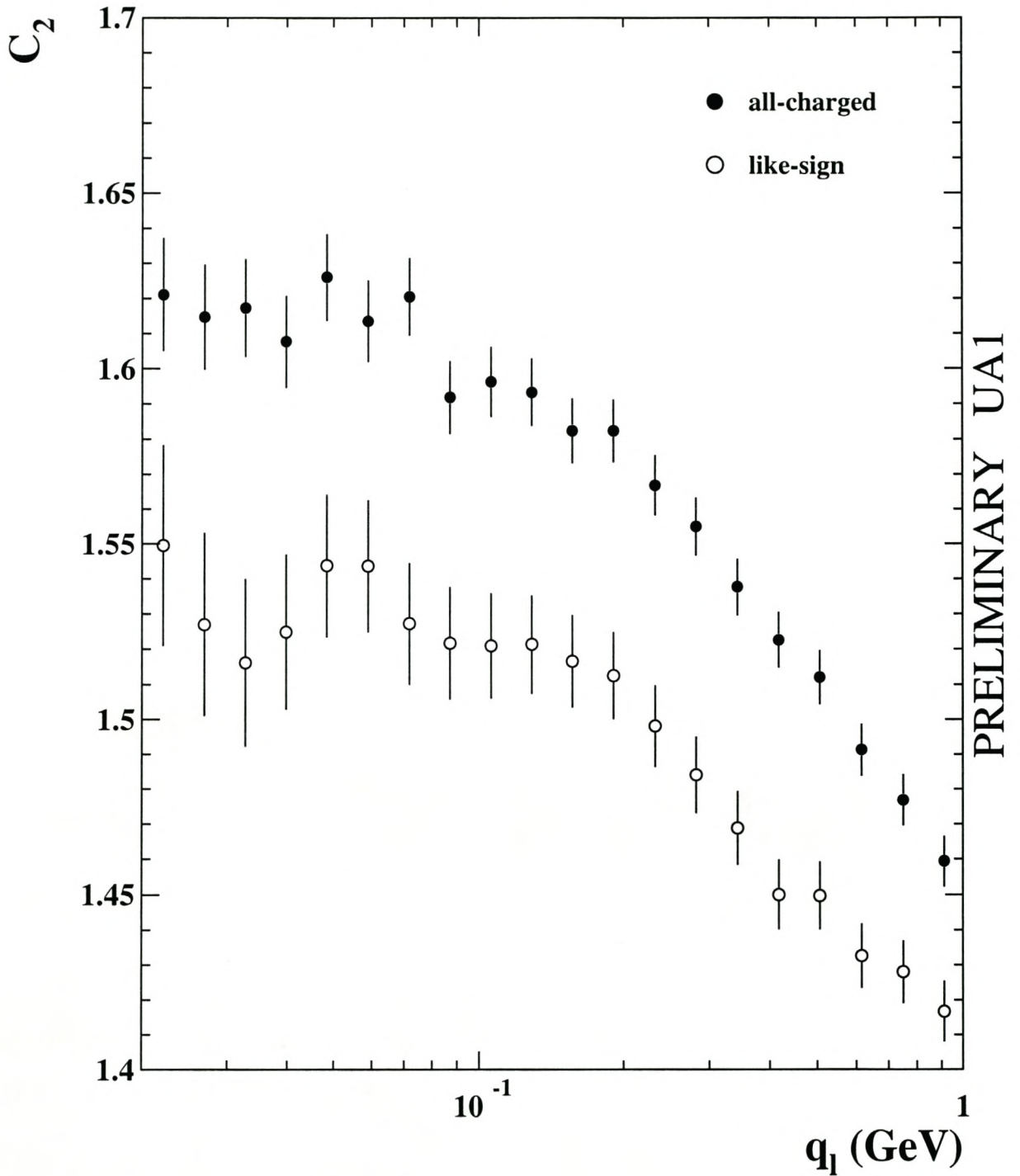


Figure 4.5: Plot of the correlation function C_2 versus q_l , the longitudinal component of the three-momentum difference, for all charged and like-sign particles.

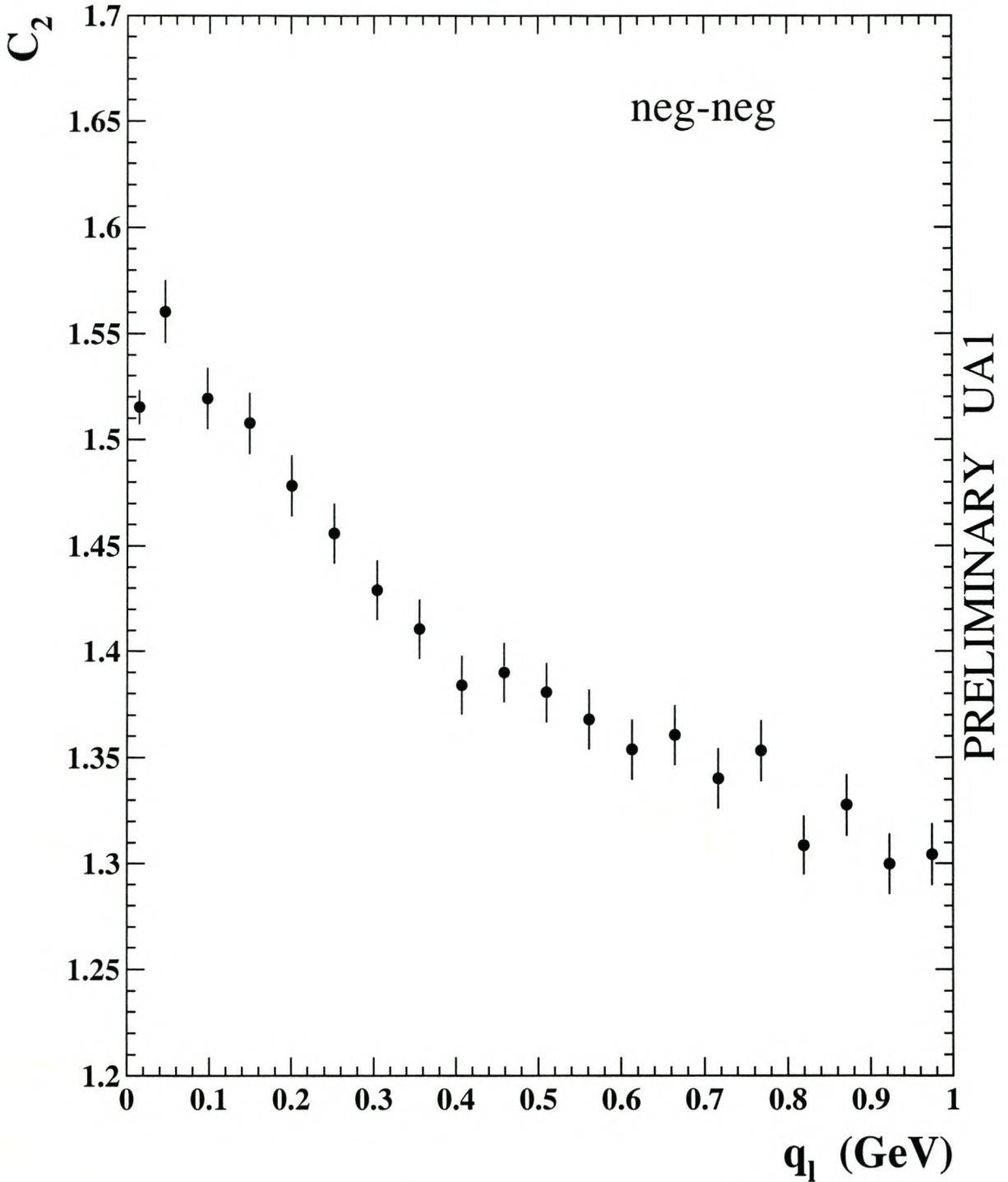


Figure 4.6: Plot of the correlation function C_2 versus q_1 for the $\pi^-\pi^-$ combination only, using linear binning over the region [0.02-1.0 GeV]. The stronger rise observed with linear binning can be contrasted with the seeming saturation shown in the logarithmic binning case of Fig. 4.5. No restriction has been placed on q_t .

As can be seen e.g. in Fig. 4.3, the overall normalization factor γ , which is the second order moment of the overall multiplicity, is ≈ 1.4 at 1 GeV. This is because the overall multiplicity distribution is not Poissonian. In the case of a Poisson distribution, $\xi_2 = \xi_1^2$, so that C_2 should be equal to one.

The one-dimensional analysis does not portray the Bose-Einstein effect all that well. Ochs [56] showed in the context of intermittency that projection onto one dimension diminishes an effect that is very clear in higher dimensions. With the single exception of the Q^2 plots (which as we have seen in Section 2.4.5 are sensitive to higher-dimensional effects) this is once again confirmed by our results.

4.2 Two-dimensional $q_t - q_l$ analysis

The two-dimensional analysis was done by binning the data in two independent \mathbf{q} -components, namely q_t and q_l , to explore the joint correlations in the transverse and longitudinal directions respectively. Linear binning was used to facilitate comparison with other experiments. As we do not have enough statistics, we analysed q_l for 20 MeV slices of q_t . The region that we covered was $0.00\text{GeV} \leq q_t \leq 0.50\text{GeV}$ and $0.00\text{GeV} \leq q_l \leq 0.50\text{GeV}$ in steps of 20 MeV. The binning gave a two-dimensional grid as shown in Fig. 4.7.

However, even after the cuts were applied as described in Section 3.2, there were still some distortions in the bin where both q_l and q_t are smaller than 0.02GeV. For this reason, this bin, indicated as the shaded region in Fig. 4.7, was not used in the fits. This was done because of the limited momentum resolution at low q values. Because only a single bin was removed, it is thus still possible to measure correlations for either q_l or q_t below 20 MeV, excluding only the case where both are below 20 MeV.

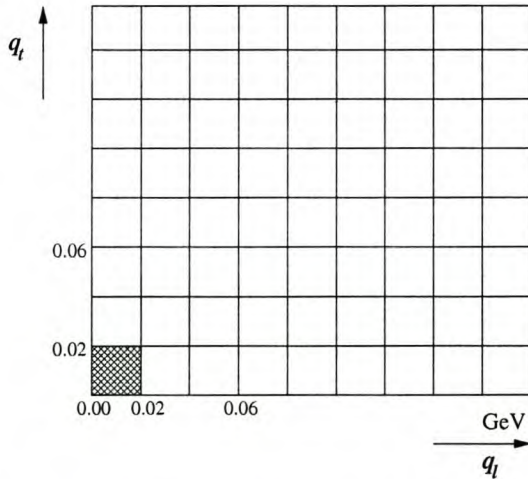


Figure 4.7: Schematic overview of binning used for measuring $C_2(q_t, q_l)$. The data points shown in subsequent figures represent each horizontal “slice” of bins, keeping q_t restricted in a narrow range while letting q_l run. The shaded bin is excluded from all fits due to the limited momentum resolution at low q_l and q_t values.

The two-particle correlations $C_2(q_t, q_l)$ were determined using Eq. (4.1). The data were then fitted with a Gaussian parametrization of the form given in Eq. (2.57)

$$C_2(q_t, q_l) = \gamma[1 + \lambda e^{-r_t^2 q_t^2 - r_l^2 q_l^2}]$$

to extract the radii parameters r_t and r_l . The two-dimensional analysis was done in the laboratory frame and the LCMS.

4.2.1 Lab frame fits

The laboratory frame which corresponds to the coordinates as shown in Fig. 3.3, was first used to analyse the data. The transverse momentum difference of the pairs of particles was calculated as $q_t = \sqrt{\Delta p_y^2 + \Delta p_z^2}$, where Δp_y and Δp_z are the differences in the y and z components of the two particles respectively. The difference in the x -components of the momentum of the two particles, defined the longitudinal momentum q_l . (Contrary to most theoretical usage, UA1 identifies the beam axis as the x axis.)

Figures 4.9 – 4.12 show the data for like-sign $C_2(q_l, q_t)$ with each plot a 20 MeV slice in q_t . In the first plot of Fig. 4.9, the leftmost point is the one that was excluded when doing the overall two-dimensional fit; it is shown only for illustration. As is to be expected, the data differs significantly from 1.4 only for small (q_l, q_t) , so that the data points become even flatter as the value of q_t is increased.

The Gaussian parametrization Eq. (2.57), was fit to all data points of Figs. 4.9 – 4.12 simultaneously (with the exception of the one excluded bin mentioned above), i.e. the best-fit values for γ , r_l and r_t are constant throughout. The following best fit values were obtained in the laboratory frame:

$$\begin{aligned}\gamma &= 1.42 \pm 0.0074 \\ \lambda &= 0.300 \pm 0.016 \\ r_l &= 0.728 \pm 0.040 \text{ fm} \\ r_t &= 0.814 \pm 0.052 \text{ fm} \\ \chi^2/\text{NDF} &= 350/620\end{aligned}$$

The value $\gamma = 1.42$ is in good agreement with previous results (see Fig. 4.3) and once again signifies the non-Poissonian character of the overall UA1 multiplicity distribution.

Judging by eyesight, the dotted line representing the best fit does a fairly good job of representing the data. We do, however, observe the same phenomenon observed for the Q^2 analysis [9], namely that for the smallest q_l, q_t values, the fit is somewhat lower than the data. For the higher q_t slices, a good correspondence is obtained between data and best fit curve.

From the output it is clear that r_t is larger than r_l , indicating an oblate source shape. This is a surprising result, given that other experiments at lower energies [22, 57], allowed for an ellipsoidal shape, but concluded that the data preferred a spherical source in the laboratory frame of reference.

In order to test the robustness of the result that $r_l < r_t$, we excluded two further data points

from the overall fit, as indicated by the shaded areas in Fig. 4.8. This restricted fit produced

$$r_l = 0.707 \pm 0.039 \text{ fm}$$

$$r_t = 0.783 \pm 0.049 \text{ fm.}$$

Although the values are somewhat smaller, the tendency remains the same with $r_l < r_t$. The ratio $r_l/r_t \approx 0.9$ remains more or less constant and does not coincide with a spherical shape ($r_l/r_t = 1$). The standard errors on r_l and r_t are small enough to conclude that the deviation from a spherical shape is statistically significant.

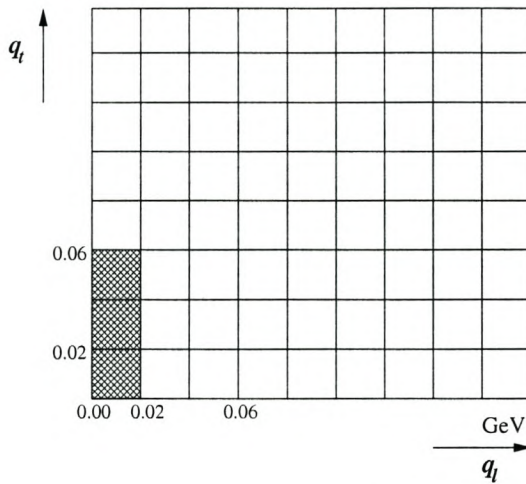


Figure 4.8: In order to test the robustness of best-fit parameters, two further bins, indicated by the shaded region were excluded from the overall fit.

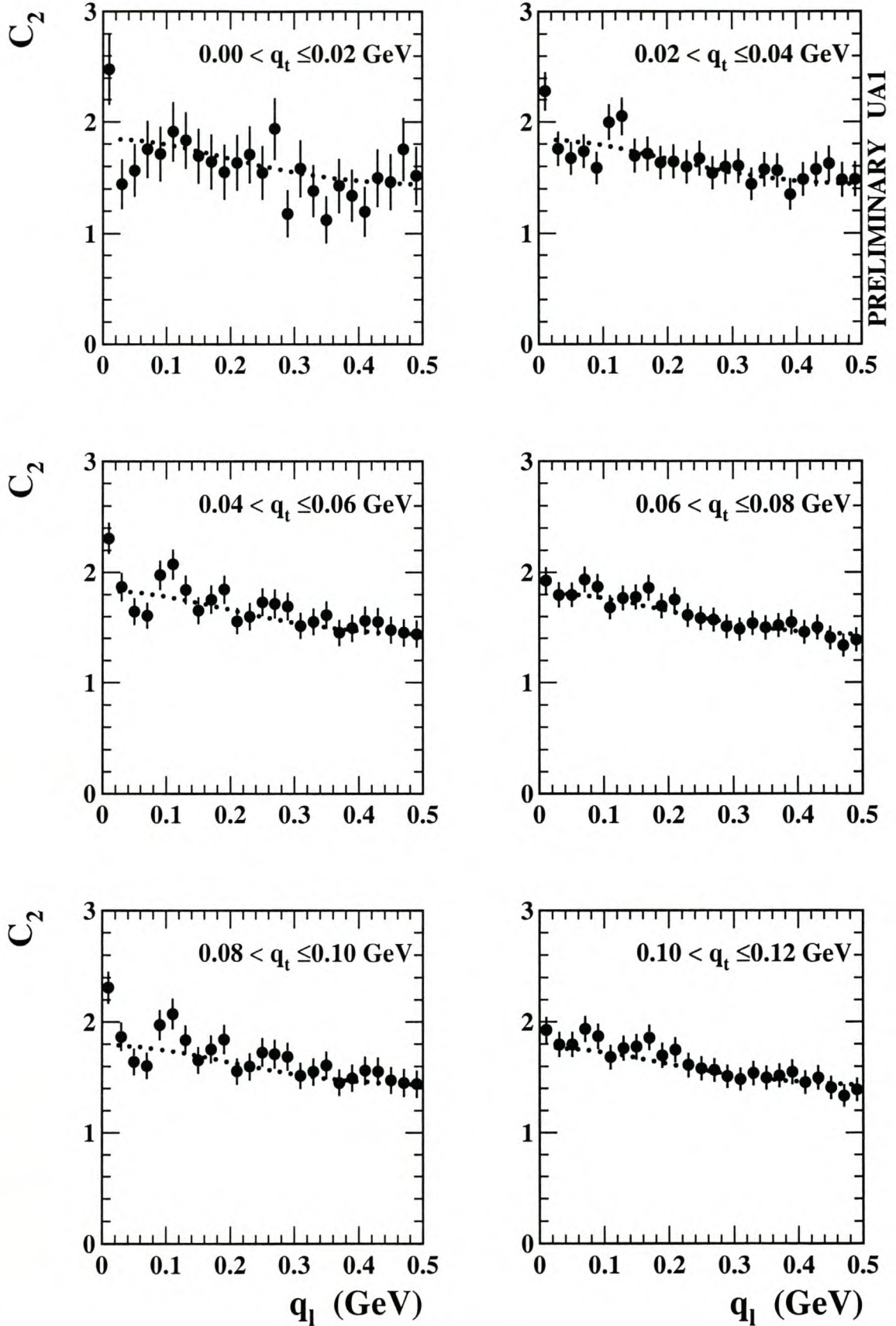


Figure 4.9: Two-dimensional correlation function for the data slice with $0.00 < q_t \leq 0.12$ GeV in the lab frame. The correlation function C_2 was determined with the parametrization of Eq. (4.1). An overall two-dimensional fit was performed for all q_t slices simultaneously, excluding only the one bin shown as the shaded region in Fig. 4.7.

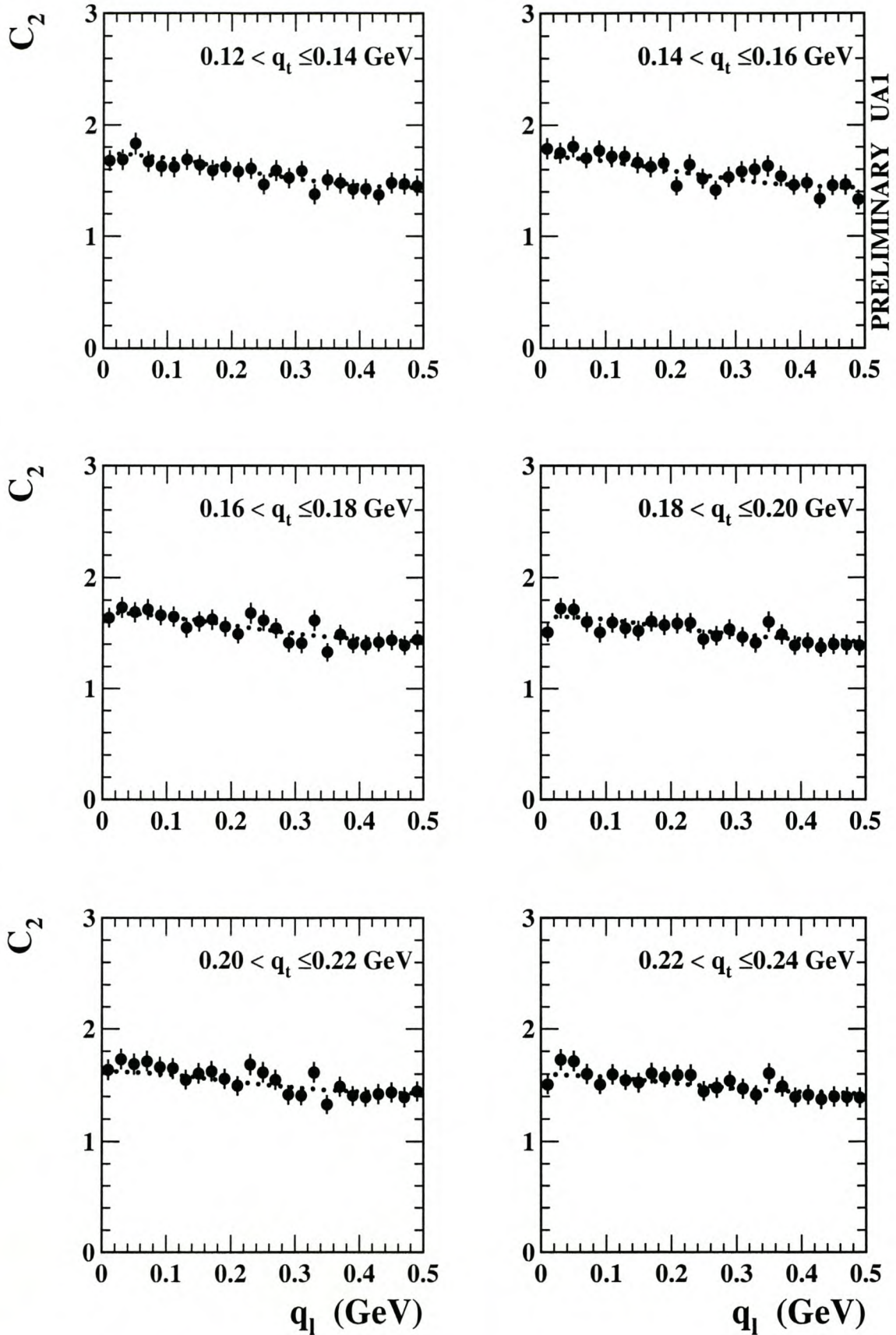


Figure 4.10: Correlation function and overall fit for data slices with $0.12 < q_t \leq 0.24$ GeV in the lab frame (continued from Fig. 4.9).

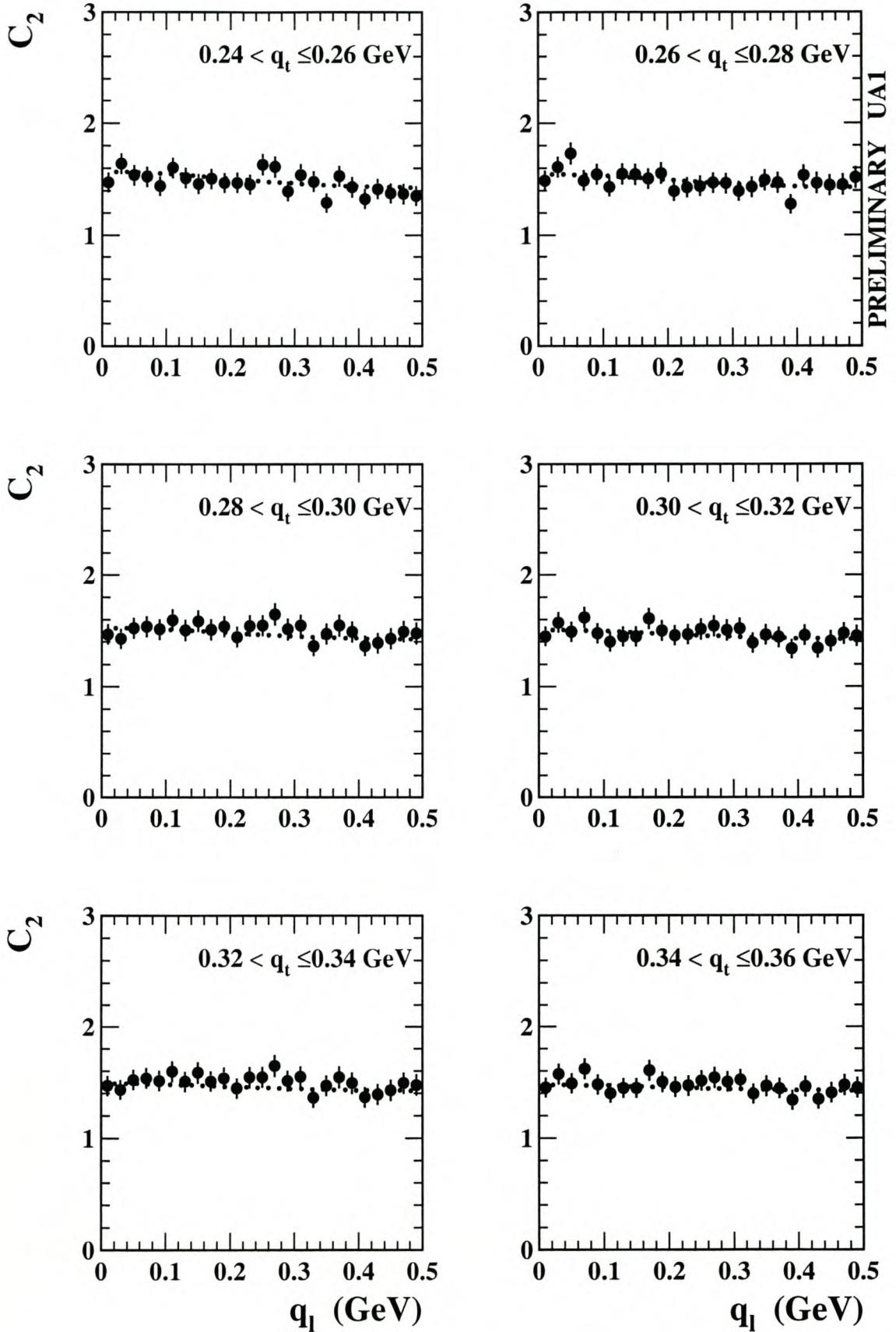


Figure 4.11: Correlation function and overall fit for data slices with $0.24 < q_t \leq 0.36$ GeV in the lab frame (continued from Fig. 4.10).

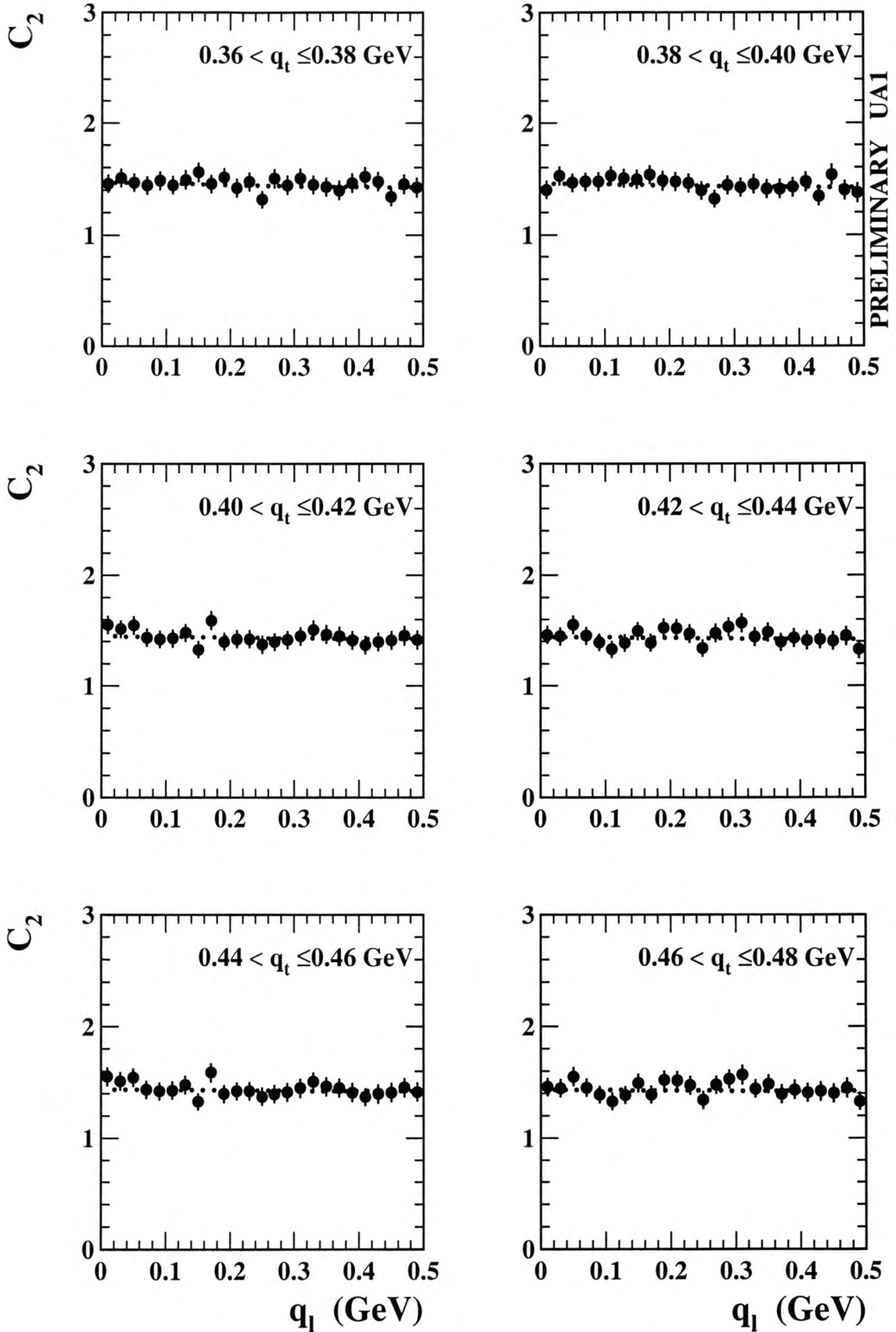


Figure 4.12: Correlation function and overall fit for data slices with $0.36 < q_t \leq 0.48$ GeV in the lab frame (continued from Fig. 4.11).

4.2.2 LCMS fits

The second frame of reference used in the analysis was the longitudinal center-of-mass system (LCMS), which was discussed in Section 2.3.4. LCMS represents an improvement in BEC studies compared to previous studies at lower energies which used the laboratory frame. It is a convenient reference frame which simplifies the interpretation of experimental radii in terms of source parameters, as was pointed out in Section 2.4.

In Figs. 4.13 – 4.16 the results for the LCMS $C_2(q_t, q_l)$ are shown with q_l being calculated according to Eqs. (2.45) and (2.46) for 20 MeV slices in q_t . The overall fit is again shown by the dotted lines on the one-dimensional data slices. The data are in good agreement with the fit results. The data in the smallest bin $0.00 < q_l \leq 0.02\text{GeV}$ for small q_l , are not completely corresponding to the Gaussian fit. For the Q^2 analysis [9], the same region didn't correspond with a Gaussian, but followed a power law.

The overall Gaussian fit, Eq. 2.57, with q_l now in the LCMS, yielded

$$\begin{aligned}\gamma &= 1.39 \pm 0.0050 \\ \lambda &= 0.336 \pm 0.013 \\ r_l &= 1.11 \pm 0.048 \text{ fm} \\ r_t &= 0.664 \pm 0.029 \text{ fm} \\ \chi^2/\text{NDF} &= 405/620.\end{aligned}$$

The incoherence parameter λ is more or less the same as in the lab frame. The transverse radius however, is now found to be significantly smaller than the longitudinal radius. This implies an elongation of the source (i.e. it is now prolate) in the direction of the collision.

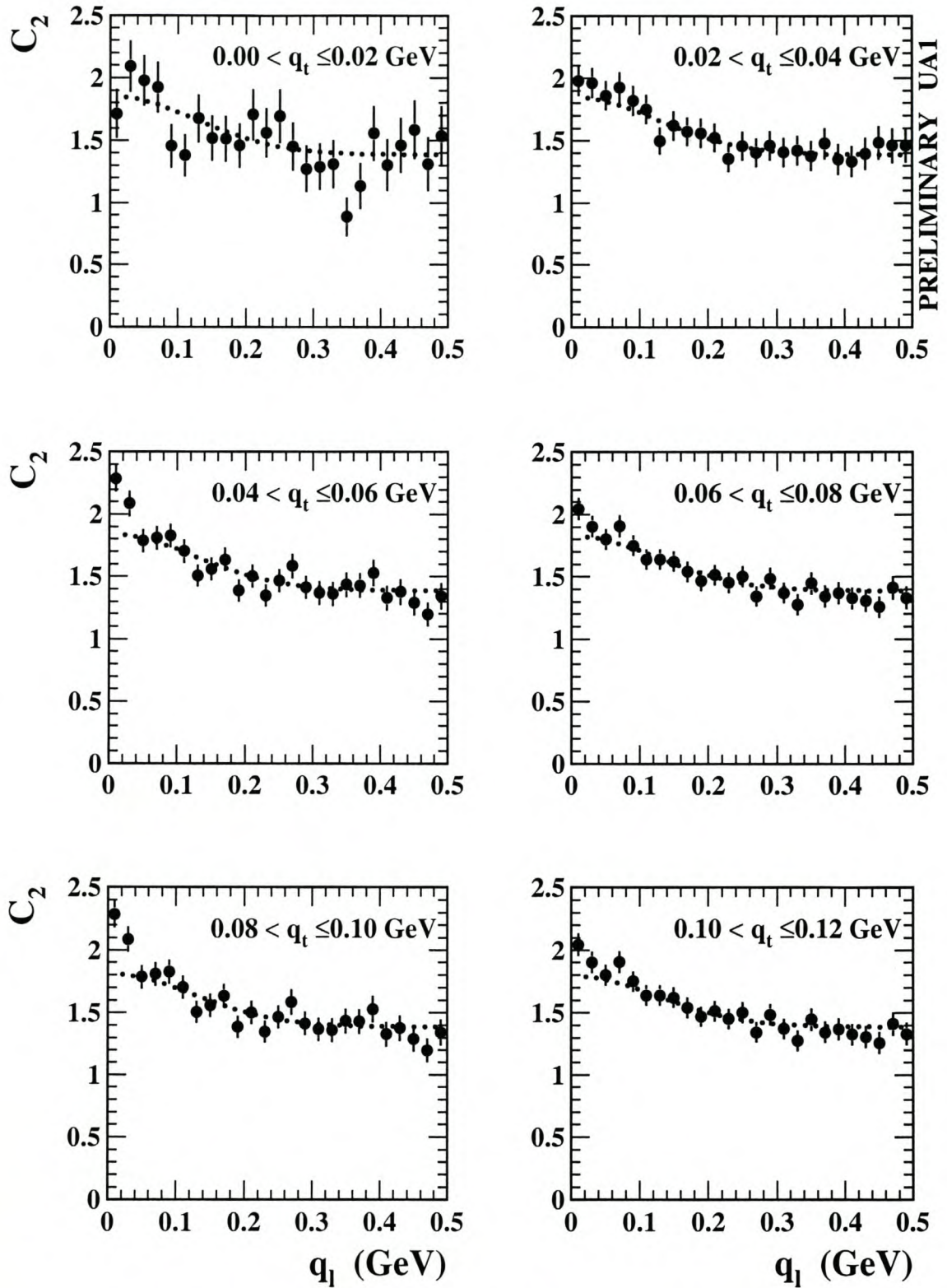


Figure 4.13: Correlation function and overall fit for data slices with $0.00 < q_t \leq 0.12$ GeV in LCMS. The correlation function C_2 was determined with the parametrization of Eq. (4.1). An overall two-dimensional fit was performed for all q_t slices simultaneously, excluding only the one bin shown as the shaded region in Fig. 4.7.

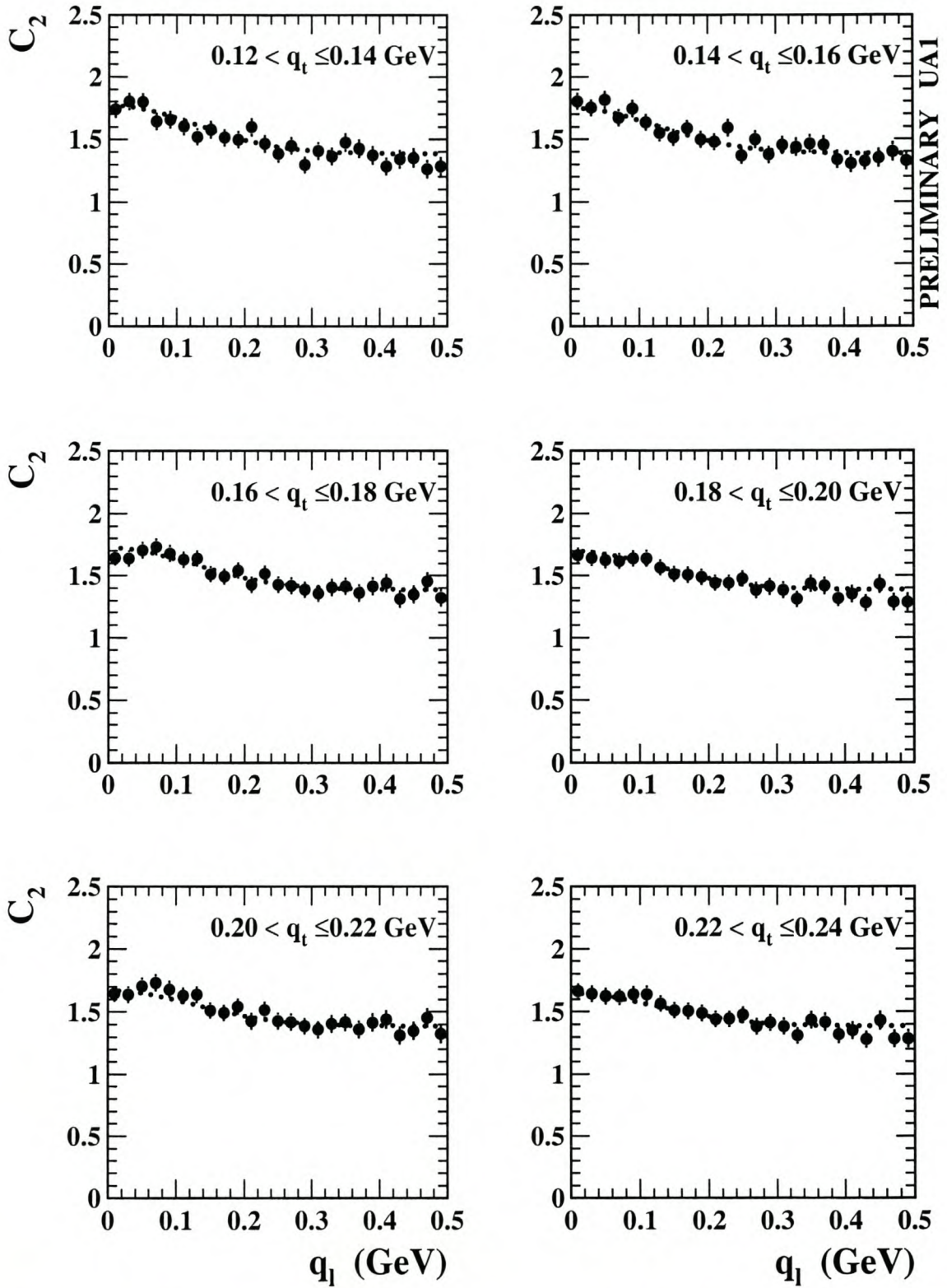


Figure 4.14: Correlation function and overall fit for data slices with $0.12 < q_t \leq 0.24$ GeV in LCMS (continued).

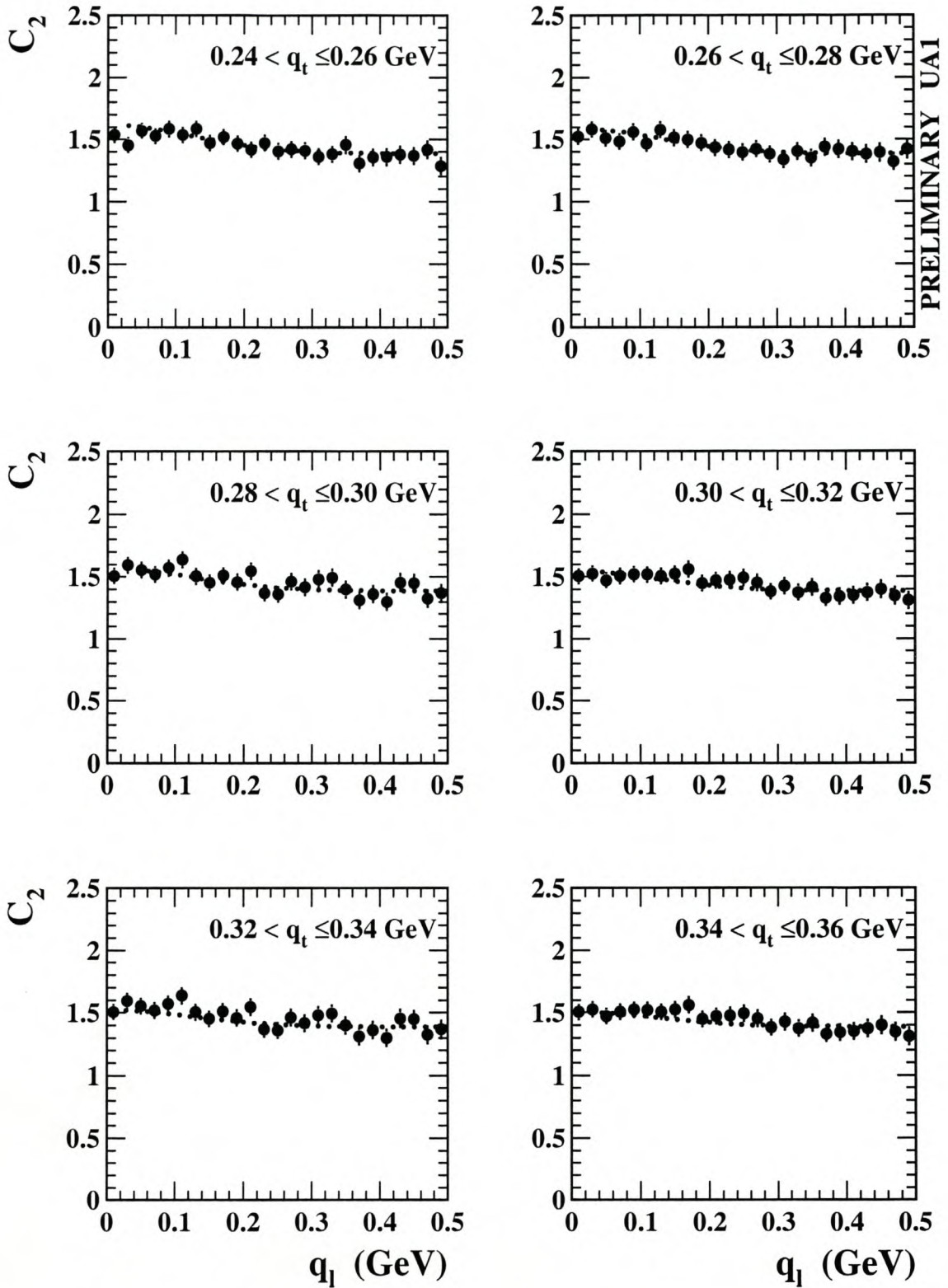


Figure 4.15: Correlation function and overall fit for data slices with $0.24 < q_t \leq 0.36$ GeV in LCMS (continued).

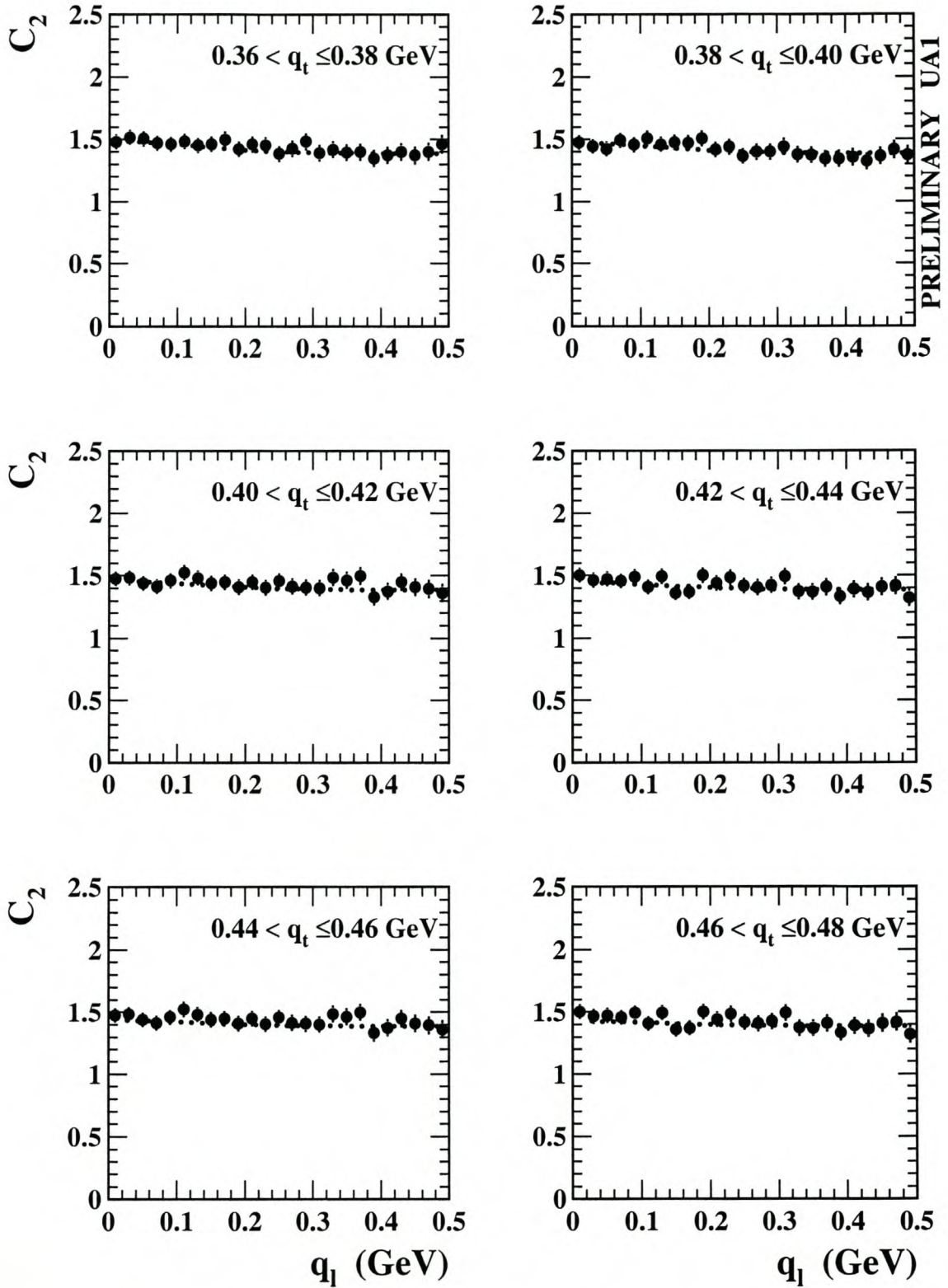


Figure 4.16: Correlation function and overall fit for data slices with $0.36 < q_t \leq 0.48$ GeV in LCMS (continued).

4.2.3 Comparison with other experiments

Our LCMS result that $r_l > r_t$ compares well with that of other experiments such as NA22 [34], DELPHI [58], OPAL [59] and L3 [60] as shown in Table 4.1. NA22 is also a hadron-hadron experiment (we standardized its quoted radius parameters in order to make comparisons useful) while DELPHI, OPAL and L3 consider final states arising from e^+e^- collisions at LEP. The results from the three LEP experiments are consistent with an elongation of the source. In heavy ion collisions at the SPS, a prolate shape with $r_l > r_t$ (where r_t is taken to correspond more or less to r_s and r_o , the side and out radii in the transverse plane) is also observed [61, 62, 63].

4.2.4 Space-momentum correlations and lengths of homogeneity

In considering the implications of the source elongation, it is important to discuss the origin and meaning of the concept of “length of homogeneity”. As discussed in Chapter 2, HBT analysis of a static source would yield source parameters that correspond directly to the source size. When the source is expanding, however, and especially when there are correlations between space and momentum coordinates of the source, the situation is considerably more complicated, since then the “radii” measured by HBT, which rely on measuring the half-width of relative momentum spectra, get to see only certain pieces of the source at a time, depending on the sum of the pair momenta \mathbf{K} . HBT thus measures this extent of the spatial size over which momentum distributions still overlap significantly, i.e. the length of homogeneity.

Very strong space-momentum correlations are, however, present in almost all high-energy collisions, since in the hadronic and nucleus-nucleus cases the colliding projectiles draw out regions of deconfinement between the leading baryons as they move apart after collision. This behaviour, first sketched by Bjorken [64], is commonly accepted as a departure point for analysis, and implies that very strong space-momentum correlations can be assumed. The “boomerang shape” of the longitudinal emission function observed by NA22 and heavy ion theorists on reconstructing the emission function [65, 66] illustrates this very well.

UA1 data has similar space-momentum correlations, and the longitudinal radius is thus also to be interpreted as a length of homogeneity. The discussion on the issue whether $r_l > r_t$ or vice versa therefore includes considerations of flow and overlap of momentum distributions, both in the longitudinal and transverse directions. A deeper understanding of these would need more detailed analysis of HBT radii as functions of \mathbf{K} , or at least rapidity y and transverse mass m_\perp .

The difference in measured radii are also in qualitative agreement with the theoretical predictions of the string fragmentation model [67], according to which the longitudinal correlation length in hadronic decay is expected to be larger than the transverse one.

	UA1	UA1	NA22 ^a	DELPHI	OPAL	L3
Colliding system	$p\bar{p}$	$p\bar{p}$	$(\pi^+/K^+)p$	e^+e^-	e^+e^-	e^+e^-
\sqrt{s} (GeV)	630	630	22	91.2	91.2	91.2
Reference frame	Lab	LCMS	LCMS	LCMS	LCMS	LCMS
γ	1.42 ± 0.0074	1.39 ± 0.0050	0.968 ± 0.011	unknown	0.842 ± 0.001	$\approx \text{unity}$
λ	0.300 ± 0.016	0.336 ± 0.013	0.471 ± 0.021	0.261 ± 0.007	0.442 ± 0.004	0.41 ± 0.01
r_l (fm)	0.728 ± 0.04	1.11 ± 0.05	0.870 ± 0.06	0.85 ± 0.08	1.018 ± 0.009	0.74 ± 0.02
r_t (fm)	0.814 ± 0.052	0.664 ± 0.029	0.63 ± 0.04	0.53 ± 0.08	–	–
r_s (fm)	–	–	–	–	0.809 ± 0.006	0.59 ± 0.01
r_o (fm)	–	–	–	–	0.536 ± 0.006	0.53 ± 0.02
χ^2/NDF	350/620	405/620	603/619	96/92	34632/24428	2314/2189

^aThe radii have been standardized

Table 4.1: Comparison of source parameters obtained by fitting a Gaussian function in two or three dimensions to the data. The results of UA1 are compared with other experiments such as NA22, DELPHI, OPAL and L3. An elongation of the source is observed in the LCMS. All the errors quoted are statistical.

4.2.5 Source elongation and Lorentz transformations

We return to the difference in shape observed in the lab and LCMS frames, represented by the relative sizes of r_l and r_t . The effect on these radii of the Lorentz transformation between the systems must be understood before other possible causes for changes are investigated.

Things are simple, it seems: under a longitudinal boost only the longitudinal momenta and energies change, while transverse momentum and all associated transverse variables (\mathbf{q}_t , \mathbf{K}_t , m_\perp , etc) remain constant. So one would expect that r_l would also change with a boost, causing r_l to be Lorentz contracted in the lab frame, while r_t should stay the same.

This, however, is not the case: The transverse radius r_t diminishes in the LCMS compared to the lab system ($r_{t(LCMS)} < r_{t(lab)}$). While one possible explanation may lie in the purely experimental uncertainties of data analysis, at least one consideration should maybe be investigated further. The radius r_t depends on β_t (Eq. (2.58)) which is a function of the energies

$$\beta_t(E_1, E_2) = \frac{K_t}{E_1 + E_2}.$$

The energies in turn depend on the longitudinal components that are subject to change

$$E_i(q_l, \mathbf{q}_t, K_l, \mathbf{K}_t) = \sqrt{p_{il}^2 + \mathbf{p}_{it}^2 + m^2} = \sqrt{\frac{1}{4}q_l^2 + K_l^2 + K_l q_l + \frac{1}{4}\mathbf{q}_t^2 + \mathbf{K}_t^2 + \mathbf{K}_t \cdot \mathbf{q}_t + m^2}.$$

There is thus no good foundation to a view that r_t should remain invariant under a longitudinal Lorentz boost.

From Eq. (2.58) it can also be seen that the transverse radius is dependent on the characteristic source time t . As time is not invariant under Lorentz transformations, it may also cause the transverse radius to change.

CHAPTER 5 CONCLUSIONS

UA1 (1985) data for $p\bar{p}$ collisions at $\sqrt{s} = 630$ GeV were analysed to determine the shape of the pion emitting source. For this, the transverse and longitudinal components q_t and q_l of the momentum difference \mathbf{q} were used. A two-dimensional fit to the data was made, using the Gaussian parametrization

$$C_2(q_t, q_l) = \gamma[1 + \lambda e^{-r_t^2 q_t^2 - r_l^2 q_l^2}].$$

The analysis was done in two reference frames, namely the laboratory frame and the Longitudinal Center-of-Mass System (LCMS).

First the one-dimensional analysis with q_t and q_l was made to confirm the BEC effect in the small region of the variables. Comparing it to other one-dimensional variables, shows the same tendency, that is, a rise in the small phase space region.

The results of the two-dimensional fit of these variables showed that the longitudinal radius is shorter than the transverse one, $r_l < r_t$, in the lab frame. This implies an oblate form of the source, meaning there could be expansion in the transverse direction. This is contrary to previous results at low energies, which found a spherical shape of the source.

In the LCMS, the longitudinal radius was found to be larger than the transverse one ($r_l > r_t$). An elongation of the source was thus found. This is in agreement with results obtained by other hadron-hadron [34], e^+e^- [58, 59, 60] and heavy ion [61, 62, 63, 68] experiments. The elongation of the source in the LCMS is also compatible with the theoretical predictions of the string model [67] and the Bjorken tube [64].

The contrast between the results obtained in these two frames of reference clearly demands explanation. Such an explanation has two aspects: Firstly, to explain a change in radius, an understanding of factors that can influence it is needed. Secondly, the role of the frame of reference and the transformation between them must be considered.

In the following, we first look briefly into the topic of Lorentz transformations, and then proceed to list a number of factors which can influence the values obtained for source parameters, without attempting to go into detail. The latter can also be interpreted as a To-Do list to be taken up in future work.

5.1 The role of frames of reference

The longitudinal Lorentz transformation from the laboratory frame to the LCMS has an influence on the longitudinal, as well as the transverse radius parameter. The Lorentz contraction

of the longitudinal radius in the lab system is the root cause of the observation that $r_{l(lab)} < r_{l(LCMS)}$. Although the longitudinal Lorentz transformation leaves the transverse component q_t unchanged, r_t also changes ($r_{t(lab)} > r_{t(LCMS)}$). Possible explanations for the change in r_t are given in Section 4.2.5.

5.2 Some factors affecting source parameters

Apart from the obvious dependence of the radius parameters on the measured $C_2(q_l, q_t)$, they are influenced by a number of factors which are sometimes easily identified but often not.

1. The dependence of the radii on the **average pair momentum \mathbf{K}** , clearly has an influence on the interpretation of the results. In Ref. [36] it was shown that the radius as a function of \mathbf{K} , is a monotonically decreasing function which decreases faster as the ratio of energy in collective expansion to thermal energy is increased. Without expansion velocity, the radius is a constant. This means that faster pions are more likely to be emitted near the point on the shell expanding with velocity in the direction of \mathbf{K} . In our analysis we implicitly integrated \mathbf{K} out.
2. The radius parameters also depend on the **transverse momentum p_t** , as shown in Ref. [53, 62]. There is a clear difference between the correlations in the low and high p_t regions. The longitudinal radius r_l demonstrates the strongest p_t dependence. The p_t dependence of the radius parameters in the experimental data is a result of the correlation between position and momentum within the source. This correlation may be caused by transverse expansion driven by rescattering of the particles in heavy ion collisions. Because of this expansion, a smaller fraction of the total source size can be probed at higher p_t .
3. Hydrodynamical models have likewise suggested that a dependence on **average transverse mass**

$$m_{\perp} = \frac{1}{2} (m_{\perp 1} + m_{\perp 2}) = \frac{1}{2} \left(\sqrt{m_1^2 + p_{t1}^2} + \sqrt{m_2^2 + p_{t2}^2} \right)$$

also has an influence on the radii parameters [68, 69]. Experimental data confirmed the model prediction of $1/\sqrt{m_{\perp}}$ dependence of the radii parameters [65]. It was found that the r_t parameter shows a weaker dependence on the transverse mass.

4. **Long-lived resonances** may also have an effect on the determination of the source size, since they cause an increase in the effective radii of the sources. In Ref. [70] it was shown that the longitudinal radius r_l is more sensitive to resonances than the transverse radius r_t . Long-lived resonances were also looked at in Ref. [71]. As we are excluding the region below 20 MeV due to momentum resolution, the halo in very small $|\mathbf{q}|$ (which results in

the large radius parameters) cannot be resolved by us, so in our analysis it will have very little effect, if any, on the resulting radius parameters [30]. Resonances such as the ρ could, however, be playing a role.

5. The dependence of r_l (CMS=lab) on the **rapidity** y , is related to the dependence of r_l on the longitudinal boost of the frame of reference in which r_l is measured. This can be seen by the expression for the rapidity as

$$y = \frac{1}{2} \ln \left(\frac{1 + \beta_l}{1 - \beta_l} \right),$$

where $\beta_l = p_l/E$ is the velocity of the longitudinal boost, with p_l the momentum of the particle in the longitudinal direction (see also Eq. (2.32)). Any dependence of the radius on β_l will thus also be visible as dependence on y . This dependence is also taken into account in the hydrodynamical parametrizations.

6. There is a linear dependence of the radii on the **multiplicity** [72]. This means that the higher the multiplicity, the larger the radii, as was also observed by UA1 [43].
7. In order to obtain a more precise shape of the source, the transverse component q_t should be decomposed into the **out and side directions** suggested in the three-dimensional Cartesian parametrization.
8. The use of **higher order cumulants** has previously proven useful in testing whether certain theoretical hypotheses are consistently fulfilled by data at all orders of correlation [29]. There is little doubt that the same approach should be as useful in the context of relative three-momenta as it was in the case of Q^2 , but analytical details remain to be worked out. Also, limited statistics will play a major role for such higher-order measurements.
9. Lastly, one should always be reminded that there is no a priori reason to believe that sources should be Gaussian in shape. The choice of parametrization clearly prejudices the results that can be obtained. There have been a number of indications, confirmed in this thesis, that more complicated source shape parametrizations may need to be investigated.

REFERENCES

- [1] R. H. Brown and R. Twiss, *Nature* **177**, 27 (1956).
- [2] R. H. Brown and R. Twiss, *Nature* **178**, 1046 (1956).
- [3] G. Goldhaber, S. Goldhaber, W. Lee, and A. Pais, *Phys. Rev.* **120**, 300 (1960).
- [4] TPC Collab., H. Aihara, et al., *Phys. Rev. D* **31**, 996 (1985).
- [5] R. H. Brown and R. Q. Twiss, *Nature* **178**, 1447 (1956).
- [6] G. I. Kopylov and M. I. Podgoretskiĭ, *Sov. J. Nucl. Phys.* **15**, 219 (1972).
- [7] G. I. Kopylov, *Phys. Lett. B* **50**, 472 (1974).
- [8] G. I. Kopylov and M. I. Podgoretskiĭ, *Sov. J. Nucl. Phys.* **19**, 215 (1974).
- [9] UA1 Collab., N. Neumeister, et al., *Z. Phys. C* **60**, 633 (1993).
- [10] A. Messiah and O. Greenberg, *Phys. Rev.* **136**, B248 (1964).
- [11] W. Zajc, *Phys. Rev. C* **29**, 2173 (1984).
- [12] J. Negele and H. Orland, *Quantum Many-Particle Systems (Frontiers in Physics)* (Addison-Wesley Publishing Company, United States of America, 1988).
- [13] U. Wiedemann and U. Heinz, *Phys. Rep.* **319**, 145 (1999).
- [14] M. Gyulassy, S. Kauffmann, and L. Wilson, *Phys. Rev. C* **20**, 2267 (1979).
- [15] S. Pratt, T. Csörgő, and J. Zimányi, *Phys. Rev. C* **42**, 2646 (1990).
- [16] S. Chapman, P. Scotto, and U. Heinz, *Nucl. Phys. A* **590**, 449c (1995).
- [17] S. Chapman, P. Scotto, and U. Heinz, *Heavy Ion Physics* **1**, 1 (1995).
- [18] S. Chapman, P. Scotto, and U. Heinz, *Phys. Rev. Lett.* **74**, 4400 (1995).
- [19] T. Trainor, *Scale-Local Topological Measures*, Technical report, University of Washington Nuclear Physics Laboratory (1998).
- [20] P. Lipa, P. Carruthers, H. C. Eggers, and B. Buschbeck, *Phys. Lett. B* **285**, 300 (1992).
- [21] H. C. Eggers, P. Lipa, P. Carruthers, and B. Buschbeck, *Phys. Rev. D* **48**, 2040 (1993).
- [22] TPC Collab., H. Aihara, et al., *Phys. Rev. Lett.* **53**, 2199 (1984).

- [23] M. Lisa, Phys. Lett. B **496**, 1 (2000).
- [24] N. Neumeister and UA1 Collaboration, Master's thesis, TU Wien (1991).
- [25] I. Andreev, M. Plümer, and R. Weiner, Int. J. Mod. Phys. A **8**, 4577 (1993).
- [26] I. Andreev, B. S. M. Plümer, and R. Weiner, Phys. Rev. D **49**, 1217 (1994).
- [27] M. Biyajima et al., Prog. Theor. Phys. **84**, 931 (1990).
- [28] EHS/NA22 Collab., N. M. Agababyan, et al., Z. Phys. C **68**, 229 (1995).
- [29] H. C. Eggers, P. Lipa, and B. Buschbeck, Phys. Rev. Lett. **79**, 197 (1997).
- [30] U. Heinz, hep-ph/9806512 (1998).
- [31] T. Csörgő and S. Pratt, in *Proc. of the Workshop on Relativistic Heavy Ion Physics at Present and Future Accelerators* (Budapest, 1991), p. 75.
- [32] M. Deutschmann et al., Nucl. Phys. B **204**, 333 (1982).
- [33] EHS/NA22 Collab., N. M. Agababyan, et al., Z. Phys. C **59**, 195 (1993).
- [34] EHS/NA22 Collab., N. M. Agababyan, et al., Z. Phys. C **71**, 405 (1996).
- [35] G. Bertsch, M. Gong, and M. Tohyama, Phys. Rev. C **37**, 1896 (1988).
- [36] S. Pratt, Phys. Rev. Lett. **53**, 1219 (1984).
- [37] S. Chapman, J. Nix, and U. Heinz, Phys. Rev. C **52**, 2694 (1995).
- [38] T. Csörgő, Phys. Lett. B **347**, 354 (1995).
- [39] R. Ganz, to be published in the proceedings of the 2nd Catania Relativistic Ion studies CRIS98 (World Scientific (Singapore)); nucl-ex/9808006 (1998).
- [40] K. Morita et al., Phys. Rev. C **61**, 034904 (2000).
- [41] F. B. Yano and S. E. Koonin, Phys. Lett. B **78**, 556 (1978).
- [42] U. Heinz et al., Phys. Lett. B **382**, 181 (1996).
- [43] UA1 Collab., C. Albajar, et al., Phys. Lett. B **226**, 410 (1989).
- [44] A. Białas and B. Ziaja, Acta Phys. Polon. B **24**, 1509 (1993).
- [45] M. Pimia, Ph.D. thesis, Univ. of Helsinki (1985).
- [46] C. Cochet et al., Nucl. Instr. and Meth. A **243**, 45 (1986).

- [47] M. J. Corden et al., Nucl. Instr. and Meth. A **238**, 273 (1985).
- [48] S. Cittolin and UA1 Collab., Nucl. Instr. and Meth. A **263**, 174 (1988).
- [49] A. Astbury et al., Nucl. Instr. and Meth. A **238**, 288 (1985).
- [50] P. Lipa, Ph.D. thesis, Universität Wien (1991).
- [51] N. Neumeister et al., Phys. Lett. B **275**, 186 (1992).
- [52] B. Buschbeck, private communication (2001).
- [53] B. Buschbeck and H. Eggers, Nucl. Phys. B (Proc. Suppl.) **92**, 235 (2001).
- [54] F. Botterweck, Ph.D. thesis, Univ. of Nijmegen (1992).
- [55] W. Kittel, hep-ph/0110088 (2001).
- [56] W. Ochs, Phys. Lett. B **247**, 101 (1990).
- [57] MarkII Collab., I. Juricic, et al., Phys. Rev. D **39**, 1 (1989).
- [58] DELPHI Collab., P. Abreu, et al., Phys. Lett. B **471**, 460 (2000).
- [59] OPAL Collab., G. Abbiendi, et al., Eur. Phys. J. C **16**, 423 (2000).
- [60] L3 Collab., M. Acciarri, et al., Phys. Lett. B **458**, 517 (1999).
- [61] NA49 Collab., H. Appelshäuser, et al., Eur. Phys. J. C **2**, 661 (1998).
- [62] NA35 Collab., T. Alber, et al., Phys. Rev. Lett. **74**, 1303 (1995).
- [63] WA98 Collab., M. Aggarwal, et al., Eur. Phys. J. C **16**, 445 (2000).
- [64] J. D. Bjorken, Phys. Rev. D **27**, 140 (1983).
- [65] EHS/NA22 Collab., N. M. Agababyan, et al., Phys. Lett. B **422**, 359 (1998).
- [66] A. Ster, T. Csörgő, and B. Lörstad, Nucl. Phys. A **661**, 419 (1999).
- [67] B. Andersson and M. Ringner, Nucl. Phys. B **513**, 627 (1998).
- [68] NA44 Collab., H. Beker, et al., Phys. Rev. Lett. **74**, 3340 (1995).
- [69] B. Lörstad, in *Correlations and Fluctuations '98: From QCD to particle interferometry*, edited by R. Hwa, T. Csörgő, S. Hegyi and G. Jancso (World Scientific, 1998), pp. 156–167.
- [70] J. Bolz et al., Phys. Rev. D **47**, 3860 (1993).
- [71] T. Csörgő and S. Hegyi, Phys. Lett. B **489**, 15 (2000).
- [72] B. Buschbeck, H. Eggers, and P. Lipa, Phys. Lett. B **481**, 187 (2000).